

ShadowCam Instrument and Investigation Overview

Mark Southwick Robinson^{1†}, Scott Michael Brylow², Michael Alan Caplinger²,
Lynn Marie Carter³, Matthew John Clark², Brett Wilcox Denevi⁴, Nicholas Michael Estes¹,
David Carl Humm⁵, Prasun Mahanti¹, Douglas Arden Peckham², Michael Andrew Ravine²,
Jacob Andrieu Schaffner², Emerson Jacob Speyerer¹, Robert Vernon Wagner¹

¹School of Earth and Space Exploration, Arizona State University, Tempe, AZ 85287, USA

²Malin Space Science Systems, San Diego, CA 92121, USA

³Lunar and Planetary Laboratory, University of Arizona, Tucson, AZ 85721, USA

⁴Applied Physics Laboratory, Johns Hopkins University, Laurel, MD 20723, USA

⁵Space Image Calibration Consulting, Annapolis, MD 21401, USA

ShadowCam is a National Aeronautics and Space Administration Advanced Exploration Systems funded instrument hosted onboard the Korea Aerospace Research Institute (KARI) Korea Pathfinder Lunar Orbiter (KPLO) satellite. By collecting high-resolution images of permanently shadowed regions (PSRs), ShadowCam will provide critical information about the distribution and accessibility of water ice and other volatiles at spatial scales (1.7 m/pixel) required to mitigate risks and maximize the results of future exploration activities. The PSRs never see direct sunlight and are illuminated only by light reflected from nearby topographic highs. Since secondary illumination is very dim, ShadowCam was designed to be over 200 times more sensitive than previous imagers like the Lunar Reconnaissance Orbiter Camera Narrow Angle Camera (LROC NAC). ShadowCam images thus allow for unprecedented views into the shadows, but saturate while imaging sunlit terrain.

Keywords: permanently shadowed regions, lunar exploration, Danuri, Korea Pathfinder Lunar Orbiter (KPLO), ShadowCam, instrument description

1. INTRODUCTION

Lunar permanently shadowed regions (PSRs) may be some of the most valuable real estate in the Solar System (Spudis 2016). They offer a unique environment with the potential for cold-trapped volatiles, including water ice, providing essential resources to enable future exploration of the Moon and beyond and provide new insight into the origin of volatiles and their delivery to the inner Solar System (Pendleton 2015; Prem et al. 2015; Deutsch et al. 2021; Feder 2021; Honniball et al. 2022; Laferriere et al. 2022; Lucey et al. 2022; Trang et al. 2022; Wilcoski et al. 2022). However, the investigation of PSRs in terms of their resource and scientific potential is still in its infancy. Various

observations have accurately delimited the locations of PSRs (Shoemaker et al. 1994; Bussey et al. 1999, 2003, 2010; Noda et al. 2008; BusseyMazarico et al. 2011; Zuber et al. 2012; Gläser et al. 2014; Hayne et al. 2021; Schorghofer et al. 2021) and thermal observations indicate where various volatiles are thermally stable within PSRs (Zhang & Paige 2009; Paige et al. 2010; Gläser et al. 2021). These observations of where water ice could be stable do not perfectly correlate with where the sum of currently available measurements suggest ice is located (e.g., from neutron absorption (Feldman et al. 2000, 2001; Mitrofanov et al. 2010; Miller et al. 2014), or reflectance variations (e.g., Gladstone et al. 2012; Lucey et al. 2014; Li et al. 2018, see reviews in Brown et al. 2022; Lucey et al. 2022), or topographic anomalies (Figuera et al. 2022).

© This is an Open Access article distributed under the terms of the Creative Commons Attribution Non-Commercial License (<https://creativecommons.org/licenses/by-nc/3.0/>) which permits unrestricted non-commercial use, distribution, and reproduction in any medium, provided the original work is properly cited.

Received 06 OCT 2023 Revised 21 NOV 2023 Accepted 23 NOV 2023

†Corresponding Author

Tel: +01-480-727-9691, E-mail: robinson@ser.asu.edu

ORCID: <https://orcid.org/0000-0001-9964-2932>

To make substantial additional progress in understanding the origin, extent, concentration, utility, and accessibility of volatiles contained within PSRs, landed missions are required (Beyer et al. 2023; Martin et al. 2023). Thus we proposed ShadowCam, a focused imaging investigation of PSRs that will provide critical information about landforms and traversability, and search for evidence of spatial and temporal variability in volatiles at scales required for upcoming landed exploration.

The hypothesis that cold-trapped volatiles may exist in significant quantities within lunar PSRs (Watson et al. 1961; Arnold 1979; Ingersoll et al. 1992) provided the initial impetus to investigate the lunar poles with remote sensing experiments. The implications of such measurements are still being assessed. Neutron absorption measurements from Lunar Prospector and the Lunar Exploration Neutron Detector (LEND) provided definitive measurements of large-scale hydrogen sequestration within polar regions (Feldman et al. 1998, 2000, 2001; Elphic et al. 2007; Mitrofanov et al. 2010, 2012; Boynton et al. 2012; Litvak et al. 2012). Bistatic radar measurements of a coherent backscatter effect at low phase angles hinted at the possibility of ice deposits in or near Shackleton and Cabeus craters (Nozette et al. 1996, 2001; Patterson et al. 2017). However, studies of radar backscatter and polarization properties suggest the radar signatures within PSRs could all be attributed to rock strewn crater deposits, rather than ice, and show no difference from sunlit regions (e.g., Campbell et al. 2006). Interpretations of observations from synthetic aperture radar (SAR) measurements obtained by the Chandrayaan-1 Mini-SAR and the Lunar Reconnaissance Orbiter (LRO) Mini-RF again suggested ice-rich deposits were likely present when geologic context was considered (Spudis et al. 2010, 2013), though the inherent ambiguity between rocky and icy deposits remained (e.g., Thomson et al. 2012).

While neutron absorption and radar measurements interrogate the upper meter of the regolith, measurements that reveal only surface properties also provide results that suggest the lunar volatile story is not simple. The LRO Lyman Alpha Mapping Project (LAMP) found evidence for surface frost and high porosity in PSRs through measurements of far-ultraviolet reflectance (Gladstone et al. 2012; Mandt et al. 2016). These regions appear to be restricted to locations where measurements from Diviner show that the local temperatures never rise above 110K, the cold-trap temperature for water ice (Hayne et al. 2015). Observations from the Lunar Orbiter Laser Altimeter (LOLA) show PSRs have elevated albedo (Lucey et al. 2014), and albedo increases with decreasing temperature (Fisher et al. 2016) also consistent with (but not definitive of) the

presence of surface volatiles. However, evidence for frost is not found in all locations where water is thermally stable. There is also a poor correlation between locations where LAMP and LOLA data suggest frost is present and locations of enhanced hydrogen detected in LEND collimated data, and some regions of enhanced hydrogen are located where ice is not thought to be thermally stable at any depth (Mitrofanov et al. 2010, 2012; Sanin et al. 2012; Brown et al. 2022; Schorghofer 2022). Despite detection of ~5 wt% water at the LCROSS impact site (Colaprete et al. 2010; Neish et al. 2011), the overall locations, abundances, and form of volatiles at the lunar poles are still uncertain.

Most of the Moon has now been imaged at pixel scales better than 2 m (and as small as 25 cm/pixel) by the Lunar Reconnaissance Orbiter Camera (LROC) (Robinson et al. 2010), and additional sub-meter-scale images are being acquired by the Orbiter High Resolution Camera (OHRC) on the Chandrayaan-2 spacecraft (Chowdhury et al. 2019) and the Lunar Terrain Imager (LUTI) onboard the Korean Pathfinder Lunar Orbiter (KPLO) (Shin et al. 2018), also known as Danuri. The key exception is PSRs, owing to the difficulty of imaging in conditions where the only illumination is scattered from nearby high-standing terrain in direct sunlight (upper crater walls, massifs). The LROC team carried out a best-effort campaign to image the interior of all PSRs larger than 20 km² (and PSR-analog craters at lower latitudes) with the Narrow Angle Cameras (NAC), albeit at moderate resolution (10–40 m/pixel) and less-than-optimal S/N (< 20). The relatively low resolution of these LROC images is due to the longer exposure times (20–80 times greater than nominal) required for secondary illumination imaging in PSRs, which results in substantial down-track smear so that pixels are highly elongated (typically with an aspect ratio of 1:29; Fig. 1) (Koeber & Robinson 2013; Koeber et al. 2014; Brown et al. 2022). Within NAC shadowed images, high-reflectance ejecta of fresh craters, boulder tracks, and landslides breccias have been identified, indicating strong reflective anomalies (contrast ~2) can be confidently identified in PSRs (Koeber & Robinson 2013; Koeber et al. 2014; Brown et al. 2022). However, within current S/N limitations, no reflective anomalies detected in LROC NAC images have been definitively attributed to water frost.

Limited PSR imaging from the Kaguya Terrain Camera (Haruyama et al. 2008) and OHRC (two images; Dagar et al. 2023) have also been published. Thus, little information is available concerning the surface properties (morphology and albedo) of PSRs at exploration scales (< 10 m). ShadowCam can fill this knowledge gap and provide further insight into the polar terrain and the presence of surface volatiles.

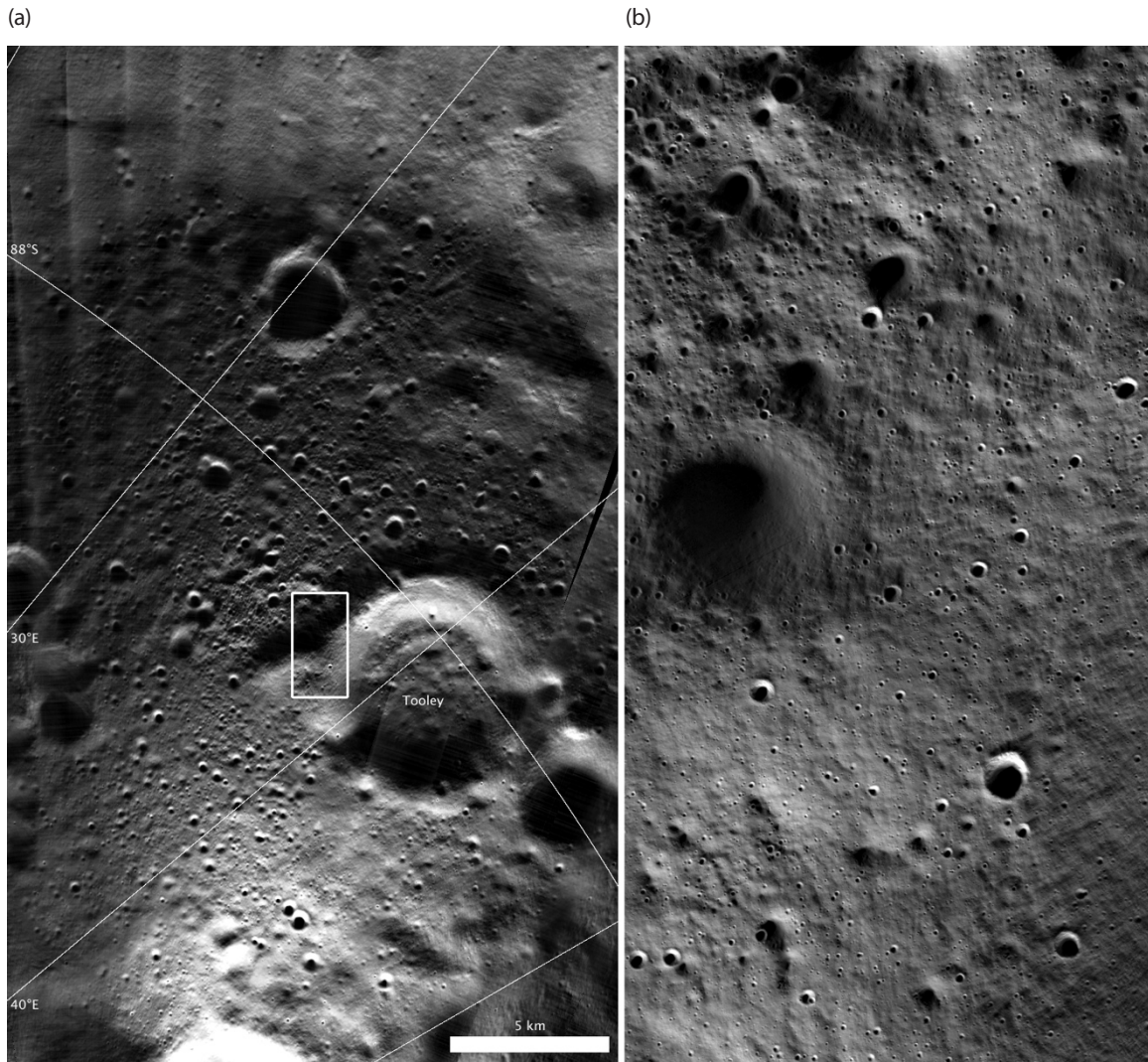


Fig. 1. Example of improvement of ShadowCam resolving power relative to LROC NAC. (a) LROC NAC mosaic of central floor of Shoemaker crater (area within PSR). Image acquired summed 2× cross-track with a 24.2 msec integration (40× the nominal integration time for illuminated terrain) resulting in 0.84 meter by 40 meter pixels; images map projected to 20 meter pixel scale. (b) ShadowCam image (1,660 meters wide) sampled at 2 m pixel scale, box in left panel shows location of right panel. LROC NAC, Lunar Reconnaissance Orbiter Camera Narrow Angle Camera; PSR, permanently shadowed regions.

2. INVESTIGATION GOALS AND OBJECTIVES

ShadowCam was designed to acquire high-resolution, high S/N images PSRs. The ShadowCam investigation was conceived to address a single overarching goal: obtain measurements that directly address three Advanced Exploration Systems (AES) lunar volatile Strategic Knowledge Gaps (SKGs) outlined in the KPLO solicitation (NASA 2016a,b; see Table 1 in NASA 2016a). These SKGs lead provide the rationale for the five ShadowCam science objectives (Table 1), which are also traceable to the Planetary Science Decadal Survey (NASA Advisory Council 2007; National Academies of Sciences 2011, 2022) and other community consensus priorities (e.g., National Research Council 2007).

2.1 Objective 1. Map Albedo Patterns in PSRs and Interpret Their Nature

Albedo boundaries coincident with PSR boundaries have been observed in images of Mercury and provide strong evidence for the presence of volatile-rich deposits (Chabot et al. 2014, 2016). The Mercury Laser Altimeter reflectance confirmed these albedo boundaries (Neumann et al. 2013). However, as noted above, existing images of lunar PSRs have yet to reveal distinct albedo contrasts attributed to the presence of volatiles, even though LOLA and LAMP have observed reflectance differences. Volatile-related albedo boundaries may be more readily discernible on Mercury, where the average reflectance of the regolith

Table 1. Science Traceability Matrix (assuming orbital altitude of 100 kilometers)

SKG	Science Objectives	Scientific Measurement Requirements		Instrument Requirements and Expected Performances			Mission Functional Requirements
		Observable	Measurement	Aspect of Performance	Required Value	Predicted Value	
1. Investigate the spatial and temporal distribution of OH and H ₂ O at high latitudes (KPLO SKG 1)	1.1 Map albedo patterns in PSRs and interpret their nature	Reflectance units with contrast of 5%	Surface reflectance of PSRs from scattered light				Nominal spacecraft altitude of 100 km Line-of-sight jitter < 8.5 μrad Line-of-sight drift 1.6°/s
	1.2 Determine the origin of anomalous radar signatures associated with some polar craters by revealing block populations down to 2-m diameter to discriminate between a blocky target and regolith-bound ice	Location, size, shape of landforms	Size-frequency distribution of blocks	GSD	≤ 2 m (IFOV ≤ 0.02 μrad)	1.7 m (IFOV 0.017 μrad)	
2. Monitor and model movement of volatiles towards and retention in permanently shadowed regions (KPLO SKG 3)	2.1 Document and interpret temporal changes of PSR albedo units	Imaging during different seasons, times of day	Temporal differences in PSR reflectance	MTF	≥ 0.2 at Nyquist frequency	≥ 0.22 at Nyquist frequency	Alignment < 4 mrad Scan rate knowledge 0.4%
				Smear	< 2 m (1.26 msec)	1.7 m (1.07 msec)	Downlink average of 16 gigabits/day
3. Investigate the geomorphology, accessibility, and geotechnical characteristics of cold traps (KPLO SKG 4)	3.1 Map the morphology of PSRs to search for and characterize landforms that may be indicative of permafrost-like processes	Landforms	Location, size, shape of landforms	Relative Calibration	2%	1%	Predict SPICE Definitive SPICE
	3.2 Provide hazard and trafficability information within PSRs for future landed elements	Landforms	Terrain roughness				Spacecraft slews for stereo (~20°)
		Stereo imaging	Topography at scales of 6 m				

The Aspect of Performance column lists the aspects that are most important for that objective, though all objectives benefit from all aspects of performance. The Required and Predicted Value columns only list the requirements for the most demanding objective. KPLO, Korea Path-finder Lunar Orbiter; SKG, Strategic Knowledge Gaps; PSR, permanently shadowed regions; GSD, ground sampling distance; IFOV, instantaneous field-of-view; MTF, modulation transfer function; SPICE, Spacecraft, Planet, Instrument, C-matrix, Events.

is low (0.17) compared to locations where ice is thought to be present (> 0.3) (Neumann et al. 2013). LOLA reflectance measurements show average lunar reflectance is 0.30 compared to 0.33 for PSRs (Lucey et al. 2014), suggesting albedo boundaries have lower contrast ratios than Mercury, and higher S/N images may be required to detect them. One difference between PSR reflectance measurements from imaging and laser altimeters is that the latter are acquired at 0° phase, which typically increases albedo contrasts, compared to high incidence angles that suppress contrasts due to increased sub-pixel scale shadowing (e.g., Hapke 2012). However, lighting within PSRs is from a broad source, and thus diffuse, likely mitigating the sub-pixel shadowing effect to a significant degree (Speyerer et al. 2023). Little is known about the photometric behavior of PSR materials, both in terms of broadly diffuse illumination and the reflectance properties of PSR materials. However, some laboratory measurements suggest contrast for ice intimately mixed with regolith should be higher at larger phase angles, leading to the suggestion that “orbital cameras with very high signal-to-noise ratios would be a better choice to detect particulate water ice than laser altimeters” (Yoldi et al. 2015).

Mercury also displays regions of low reflectance interpreted as organic-rich lag deposits where temperatures indicate organics are stable at the surface and ice is not (Neumann et al. 2013; Paige et al. 2013; Chabot et al. 2014; Syal et al. 2015; Chabot et al. 2016). Such low-reflectance deposits have yet to be identified on the Moon. The presence or absence of such deposits has important implications for the origin of volatiles in PSRs; organic-rich deposits are consistent with a cometary or volatile-rich asteroid source (e.g., Zhang & Paige 2009).

While there appears to be little ambiguity regarding the nature of Mercury’s polar deposits, where interpretations of reflectance at visible and NIR wavelengths, radar (e.g., Harmon & Slade 1992; Slade et al. 1992; Harmon et al. 1994, 2011), and thermal models are all in agreement, the reflectance measurements of the Moon can be interpreted as due to either water frost or a reduced rate of space weathering (Zuber et al. 2012; Lucey et al. 2014; Fisher et al. 2016). Due to environmental differences, PSRs may experience a reduced level of space weathering, exposure to which lowers surface reflectance (e.g., Hapke 2001). Reduced space weathering would manifest itself in diagnostic ways that include a combination of an overall higher reflectance, reduced contrast between rayed craters

and surrounding regolith, a difference in the density of rayed craters per unit area, and fresh ejecta extending further from its source crater on average (e.g., Grier et al. 2001; Braden & Robinson 2013).

ShadowCam measures radiance [watts per steradian per square meter ($\text{W}\cdot\text{sr}^{-1}\cdot\text{m}^{-2}$)] from the surface, rather than directly measuring reflectance. While small-scale reflectance changes can be identified in regions of uniform slope and lighting, in general the conversion of radiance to reflectance or absolute albedo is complicated due to the broad diffuse illumination within PSRs.

2.2 Objective 2. Investigate the Origin of Anomalous Radar Signatures Associated with Some Polar Craters

Some of the most exciting yet ambiguous results regarding water ice in PSRs come from radar observations. Spudis et al. (2010, 2013) noted a class of impact craters with high Circular Polarization Ratio (CPR) values found only within their interiors. High CPR values can be the result of either relatively pure ice (> cm size blocks) or rocks embedded in low-loss but non-ice, medium, and by rugged rocky surfaces (Campbell 2012; Virkki & Muinonen 2016). Because these “radar anomalous” craters are most densely located in PSRs, and the high CPR values are confined to their interior, rather than extending into the ejecta deposit as is typical for fresh craters, they were interpreted to host water ice (Spudis et al. 2010, 2013). Similarly, Thomson et al. (2012) found patchy enhancements of CPR within Shackleton crater that are consistent with either roughness differences on the crater wall or 5–10 wt% (up to 30 vol%) water ice in the uppermost meter of regolith. Discriminating between these scenarios (ice vs. rocky regolith) is essential for determining whether relatively “clean” ice is present in high abundances at or near the surface. Compared with the radar data, images will provide a new constraint on the cause of the high-CPR radar signature. Radar can penetrate the surface and is sensitive to cm-sized scatterers (smaller than the ShadowCam resolution), so the absence of surface rocks does not guarantee that the presence of ice causes a high CPR return. However, images can eliminate one of the significant uncertainties in interpreting the radar data by identifying blocks and roughness differences due to slumps, debris flows, and impact melt deposits that would produce increased CPR or identify regions where high CPR is associated with smoother surfaces. In PSR images currently available, blocks are only detectable down to diameters > 15–40 m (Mitchell et al. 2018), and extrapolating the sparse population of blocks of this size to the sizes relevant to radar data is highly uncertain. ShadowCam will

allow the detection of blocks in the > 2-meter size range. Block populations on the Moon commonly exhibit large numbers of blocks of this size, and block populations follow a fragmentation size frequency distribution; thus, extrapolating to the radar block size is reasonable (Hartmann 1969; Mitchell et al., 2018).

2.3 Objective 3. Document and Interpret Temporal Changes of PSR Albedo Units

One fascinating aspect of the lunar volatile story is the idea that their local abundance may vary on diurnal timescales (Sunshine et al. 2009; Livengood et al. 2015), as H_2O or OH may be adsorbed or absorbed on regolith grains on the surface (Clark 2009; Pieters et al. 2009; Sunshine et al. 2009) or in the shallow regolith (Livengood et al. 2015; McClanahan et al. 2015), and migrate either poleward, to be cold trapped, or toward the terminator. Within PSRs, this migration of volatiles would likely manifest as seasonal variations, where surface frosts would grow and recede as the local temperature fluctuates. High-resolution imaging can monitor changes in albedo boundaries within PSRs with the local season and surface temperature. Temporal changes in PSR albedo are also likely to be observed by comparing images acquired at different times, with the likelihood of observing such changes increasing as the interval between images increases. Results from LROC imaging suggest that in PSRs within 10° of the pole, at least one 5 m crater should form in one year, and > 1,000 other surface changes (e.g., related to secondary ejecta) ≥ 5 m will form (Speyerer et al. 2016a). Such disturbances of the regolith could expose volatiles (ice deposits have been observed in high-resolution images of newly formed craters on Mars (Dundas et al. 2014) and reveal differences in regolith properties with depth.

2.4 Objective 4. Map the Morphology of PSRs to Search for and Characterize Landforms That May Indicate Sub-Surface Volatiles

Prior to the flight of the ShadowCam instrument, our best images of PSRs poleward of 82° N, S have pixel scales of 20 meters and S/N < 40 (most with S/N < 20), so our knowledge of small-scale landforms is limited (relative to that of the rest of the Moon). Two-meter scale images can address numerous outstanding questions. For example, are the physical properties of regolith similar within PSRs and outside PSRs? This question can be addressed by characterizing boulder tracks (Bickel & Kring 2020; Sargeant et al. 2020) tree-bark texture (e.g. Kuiper 1965;

Shoemaker et al. 1966), presence or absence vs. slopes, and size of elements, orientation, and slopes of facets hosting debris flows, blockiness as a function of crater diameter and temperature, and finally the presence of landforms not seen in illuminated terrains. Determining the crater size-frequency distributions of PSR vs. non-PSR regions could reveal details of target properties (Van der Bogert et al. 2013). Stereo observations would prove most useful for comparing small crater shapes between PSRs and illuminated terrain (another test of target properties).

2.5 Objective 5. Provide Hazard and Trafficability Information within PSRs for Future Landed Elements

ShadowCam enables the detection of surface hazards (small craters, hummocky terrain, and boulders) that could impact the success of future landers and rovers and in-situ resource exploration efforts. The images of the inside of PSRs will complement the over 100,000 meter-scale NAC images acquired of the nearby illuminated terrain and permit the complete mapping of the polar region at the 2-meter meter scale. Leveraging ShadowCam and the existing NAC image catalogs, mission planners can derive traverse paths between key polar resource exploration targets as well as persistently illuminated areas (De Rosa et al. 2012; Speyerer & Robinson 2013; Speyerer et al. 2016b).

LOLA topographic point measurements at the pole are gridded at a spatial scale of 5 m (size of the laser spot) (Smith et al. 2010a,b; Barker et al. 2021). However, in the gridded Digital Terrain Model (DTM), 94% of the pixels are interpolated. While stereo observations from NAC and the KPLO LUTI can fill in gaps over illuminated terrain, they cannot fill in gaps in our topographic knowledge inside PSRs. ShadowCam can do this through stereo imaging, provided there are opportunities to roll or pitch the spacecraft. Topography derived from ShadowCam (5 m pixel scale DTMs) inside PSRs can be merged with stereo-derived topography from LROC and LUTI of the illuminated surface as well as LOLA altimeter profiles (Gläser et al. 2013). These PSR topographic measurements can be used to derive accurate slopes along optimal traverse paths into and out of PSRs (Speyerer et al. 2016b) and to precisely calculate the illumination conditions in the polar regions (Mazarico et al. 2011), which is essential for constraining thermal models of PSRs.

3. SCIENCE OBSERVATION REQUIREMENTS

The ShadowCam investigation objectives place

requirements on the hardware regarding pixel scale, modulation transfer function (MTF), smear, jitter, and sensitivity (Table 1). While all five objectives require high S/N and small pixel scales, Objectives 2 (block identification) and 5 (hazards and trafficability) drive the pixel scale requirement. Since the existing radar observations are most sensitive to 10 cm elements and the hazard analysis scale is closely related to the size of a landed asset (meter to several meters), ShadowCam was designed to obtain the smallest ground sampling distance possible within the schedule, mass, and fiscal constraints. Accurate block size-frequency distributions can be obtained with 2-meter pixel scales (block sizes measured to 3 pixels diameter and blocks detected at the pixel level) and extrapolated down to the radar size due to the consistency of fragmentation populations known from analysis of blocky lunar craters (Cintala & McBride 1995). The PSR-derived block populations will test the CPR anomalies; are they the result of ice concentrations or a blocky regolith?

Regarding hazards for landers, block detection down to 2 meters will also serve to delimit potentially dangerous areas. Specifying a pixel scale is insufficient to determine what can be discriminated; MTF, jitter, and smear are also important. Based on the LROC experience (very sharp images), we set these two parameters close to the NAC-measured values. While S/N is important for identifying blocks (S/N of 50 is sufficient), confident delimitation of subtle albedo boundaries requires S/N of 100 or more. The LOLA albedo mapping results report that some PSRs have interiors with reflectances 10% greater than non-PSR craters (Lucey et al. 2014) at the km scale. Since the LOLA measurements have zero-phase lighting (laser pulse) regardless of location, the measurement is far from as challenging as with secondary illumination in PSRs; thus ShadowCam requires an S/N of 100 or better for positive identification of these contrasts. S/N of 100 will also allow positive identification of local albedo contrasts within a single PSR down to the 3% level. Thus, Objectives 1 (albedo boundaries) and 2 (albedo change over time) drive the S/N requirement. Objective 2 may be the most sensitive to S/N as changes over time (i.e., frost migration) may be small, and the dynamic lighting environment (broad-source diffuse illumination) will complicate confident change detection (careful photometric modeling of the crater topography/lighting with LOLA gridded topography). The realized resolution of stereo-derived digital terrain models is sensitive to both pixel scale and S/N; thus, the requirements from the ShadowCam baseline objectives will allow 3×3 pixel matching and, hence, 5-meter DTM sampling (based on LROC experience; Henriksen et al. 2017). With LOLA altimetry and terrain

models of illuminated surfaces from the NAC and Terrain Camera, ShadowCam can increase our topographic knowledge inside PSRs. Such a merged product could be used to investigate the topography of various features and aid in deriving optimal traverses for future prospectors (Speyerer et al. 2016b).

4. INSTRUMENT DESCRIPTION

ShadowCam has a high heritage from the LROC NAC (Robinson et al., 2010; Humm et al. 2016; Speyerer et al., 2016c) and includes a build-to-print copy of the telescope. The instrument was designed and built at Malin Space Science Systems (MSSS), which also built the LROC NACs and twenty other cameras that have flown to four planetary bodies. The electronics are modified from the NAC design, accommodating a time delay integration (TDI) charge-coupled device (CCD) detector. TDI sensors improve image quality by cumulatively adding signals from multiple lines imaging the same area by transferring signal from one line to the next at the same speed as the target passes beneath the sensor. The ShadowCam design always exposes 32 lines (of 128 lines on the sensor) of TDI. This detector is back-illuminated, providing higher quantum efficiency (QE) and has larger pixels than the NAC. Along with the TDI, these factors give ShadowCam more than 200 times the sensitivity of the NACs.

ShadowCam has an instantaneous field of view of 17- μ radian and a swath width of 2.86° (3,072 pixels across). The internal memory buffer limits the down-track dimension to 84,992 lines. From a nominal 100 km altitude, ShadowCam will provide a pixel scale of 1.7 meters over a 5.2 \times 144.5 kilometer area. With the increased integration time enabled by the TDI detector (32 lines), the images typically have an S/N greater than 100 within high-priority PSRs. The S/N estimate was validated with PSR images acquired by the LROC NAC (Koeber et al. 2014; Brown et al. 2022). More information on the geometric aspects of the camera and radiometric calibration can be found in (Speyerer et al. 2023) and (Humm et al. 2023) that are contained in this volume (Table 2).

4.1 Optics (Heritage, Stray Light Mitigation)

The telescope is comprised of a composite metering structure, a secondary mirror assembly, and a primary mirror assembly, including the field flattener elements, bandpass filter, and a sunshade (Fig. 2).

The heritage (NAC) telescope is a 700 mm focal length,

Table 2. ShadowCam specifications

Parameter	Value
FOV	2.86°
IFOV (nadir)	17.16 μ rad
Pixel scale at 100-km altitude	1.7 meter
Max. swath size at 100-km altitude	5.2 km \times 144 km
f/#	3.6
Focal length	699.275 \pm 0.01 mm
Distortion coefficient k	0.0000174 \pm 0.00000057
Optical center location sample	1558 (1545, 1572 95% bounds)
Primary mirror diameter	195 mm
Aperture	194.4 mm
System MTF (Nyquist)	0.21
Gain	23 to 30 e ⁻ /DN
Read noise	60 e ⁻
Detector full-well (shallow, deep)	94,000; 123,000 e ⁻
S/N (@ 0.12 W/m ² /sr/um)	100
Spectral response	410–780 nm
Radiometric accuracy	1% relative, 6% absolute
Active pixels	3,072
Maximum lines	84,992
Detector digitization	12 bit, encoded to 8 bit
Data link to spacecraft	4 Mbps
Temperature sensors	4
Voltage	28 \pm 7 VDC
Peak power	9.3 W
Standby power	4.5 W
Mass	8.75 kg
Volume (length \times diameter)	118 cm \times 27 cm (incl. radiator)

See Humm et al. (2023) with CC-BY-NC for details on shallow vs. deep sides of the detector. See Table 2 of Robinson et al. (2010) for a similar table presenting LROC NAC parameters.

FOV, field of view; IFOV, instantaneous field-of-view; MTF, modulation transfer function; LROC NAC, Lunar Reconnaissance Orbiter Camera Narrow Angle Camera.

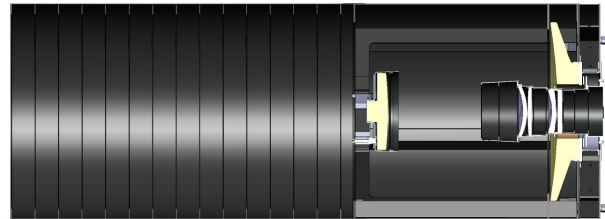


Fig. 2. The telescope consists of a sunshade, a composite metering structure, a secondary mirror assembly, and a primary mirror assembly including the field flattener elements and bandpass filter.

f/3.6 Ritchey-Chretien design with a composite metering structure and baffle (sunshade). The primary mirror is 195 mm in diameter, made of Zerodur (class 0) for thermal stability, and coated with a high-reflectance hard silver coating (Robinson et al. 2010).

Instrumental stray light was minimized by enhanced internal baffling of the telescope relative to the NAC design because of the extremely challenging target environment (dimly illuminated target regions surrounded by brightly

lit terrain). The number of internal radial baffles within the sunshade was increased from five to fifteen relative to the NAC design (Fig. 3). Additional changes were made to the secondary mirror baffle, corrector cell baffle, and detector housing – all three had added vanes to increase stray light rejection at a range of angles outside the nominal FOV. Additionally, the diameter of the corrector elements was increased to reduce total internal reflection and scatter off lens edges.

The telescope has no provision for focus adjustment in flight, so accurately determining the plane of best focus and installing the imager at that location is critical to meet the MTF requirement. Mass constraints for the LROC NAC and ShadowCam indicated a composite structure for the telescope – metering structure, sunshade, and secondary mirror mount. However, the composite material is hygroscopic and increases in length as it absorbs water. On the ground, in ambient conditions, the telescope is designed and built so that it is not focused until it is desiccated in the space environment.

Telescope focus was verified using a test collimator prior to electronics integration – this also provided a nominal position for the plane of best focus. These measurements were acquired after the tube was baked out in a vacuum chamber and before it could re-absorb moisture from the ambient environment. The ShadowCam focal plane mechanical design allows a focus spacer to be installed between the focal plane assembly (FPA), which contains the imager and the interface with the ShadowCam telescope.

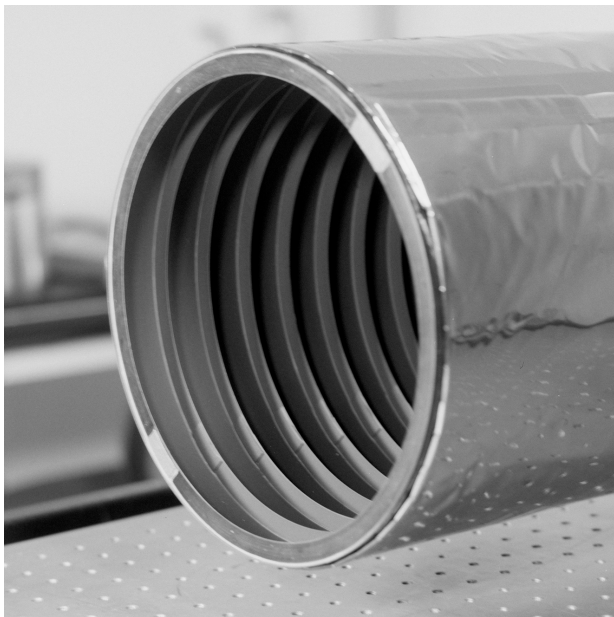


Fig. 3. Internal radial baffles within the sunshade.

This spacer can be set to the correct thickness such that the imager is in focus once in orbit.

The integrated instrument (telescope and electronics) was tested using an external collimator with optics identical to the flight telescope (Fig. 4). Before use, it was auto-collimated to infinity using a large optical flat. A bar target with a known tilt was installed in the focal plane of the collimator with a 2.3 (+/-0.2) degree tilt – that ensured that only one of the bars would be in the optimal focus position of the collimator focal plane (Humm et al. 2023). Calculations indicate which bar should be at infinity focus.

Next, the instrument was baked out, set to a flight-like temperature, and configured to image the collimated target (Fig. 4). Custom software was used to calculate the MTF across the field of the bar target image and estimate the location of optimum focus. This location was set, focus checked, and spacers were used to make small adjustments until optimal focus was found (Fig. 5).

We acquired an image of the Moon from Earth, providing a final qualitative check that the focus was set correctly (Fig. 6). Acquiring the lunar image presented several challenges. The instrument had to be scanned across the Moon at a fixed rate appropriate for the TDI line time. A neutral-density commercial filter had to be held by hand in front of the aperture while scanning the Moon to attenuate the bright Moon to a radiance within the detector range (designed to image only indirectly illuminated terrain). While this approach had several issues (including both

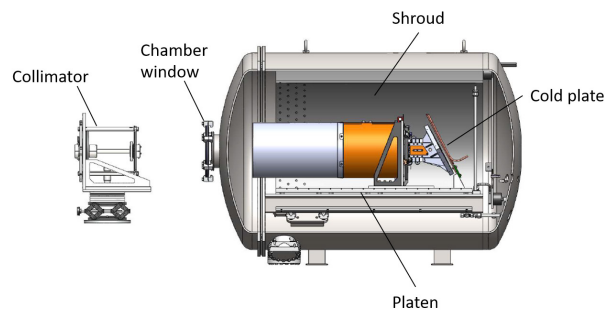


Fig. 4. ShadowCam thermal vacuum test setup.

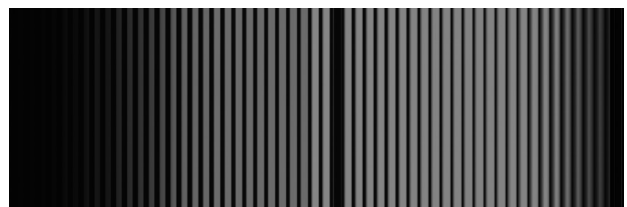


Fig. 5. ShadowCam image tilted bar target from the collimator.



Fig. 6. ShadowCam image of the Moon, taken from Earth to verify focus. The blurring in the upper left section of the image is from light scattering off of a filter held in front of the aperture. The craters in the lower right near the terminator show sharp edges, indicating the camera is in focus at infinity.

scattered and reflected light off the filter), a section of the image exhibited pixel-scale contrast consistent with the instrument in focus.

4.2 Electronics

The ShadowCam electronics are a modified version of those of the Mars Reconnaissance Orbiter Context Camera (CTX), as described in Malin et al. (2007). The LROC NAC electronics were also based on the CTX design (Robinson et al. 2010). Electronically, ShadowCam is more similar to the older CTX in terms of speed, so we will describe changes relative to that baseline.

Like CTX, the ShadowCam electronics are packaged as a single rigid-flex printed circuit board assembly (Fig. 7). Four rigid segments, each supporting its own specific function (detector, analog-to-digital converter (ADC), instrument control, and data handling, performed by the field programmable gate array (FPGA), and power conversion) are connected by flexible interfaces.

The most significant difference between ShadowCam and CTX is using an entirely different CCD image sensor (Fig. 8). For ShadowCam, the Hamamatsu S10202-08-01 image sensor was selected to increase sensitivity. This sensor is a TDI line scan CCD with 128 bidirectional TDI stages and 4096 12-micron pixels per line, read out as 524-pixel regions (512 photoactive, two pre-scan, eight bias, and two over-scan pixels) to eight separate output taps (Speyerer et al. 2023). ShadowCam uses a version of the sensor with a custom light shield, which exposes 32 lines in the center of the detector to limit the maximum signal level. Only the center six regions of the sensor are read-out, for an effective total width of 3,072 photoactive pixels.

To support the Hamamatsu sensor, the two AD1672 ADCs used in CTX were replaced with two Analog Devices AD9814 three-channel analog front ends (AFEs). Each AD9814 has three input channels and can perform Correlated Double Sampling and adjustable gain and offset to each input before digitizing to 14 bits at a maximum rate of 3.3 MSPS per channel. For ShadowCam, the two lowest-order bits are discarded, providing 12-bit pixels.

The primary system clock frequency, like CTX, is 20 MHz. The pixel loop logic uses 12 clocks to read a sampled pixel from all six channels, compand each 12-bit sample to 8 bits using a piecewise linear companding function (Humm et al. 2023), and then writes the six resulting bytes to a first in, first out buffer, which stores the data into the dynamic random access memory using bank interleaving. This serial-parallel processing results in the pixels being interleaved relative to the order of DRAM readout, and the interleaving is reversed during ground processing. The line rate can be set from 316.7 μ sec 10.35 msec in 4,096 steps.

The focal plane section of the electronics is completely

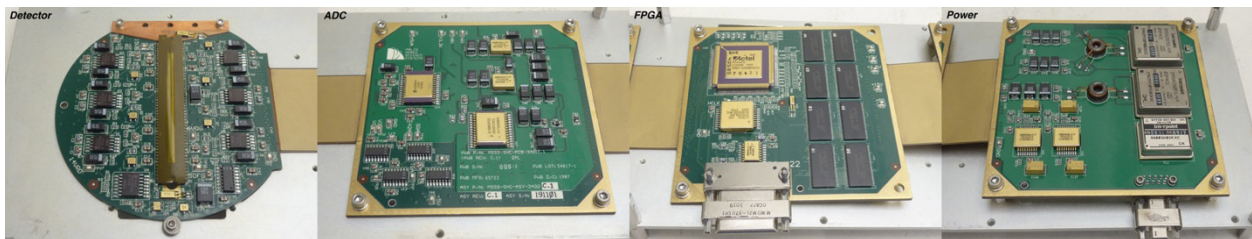


Fig. 7. The four electronic printed circuit boards connected by a flexible interface. Before integration with the telescope, the four boards are folded into a compact package (10.7 cm \times 10.7 cm \times 6.9 cm).

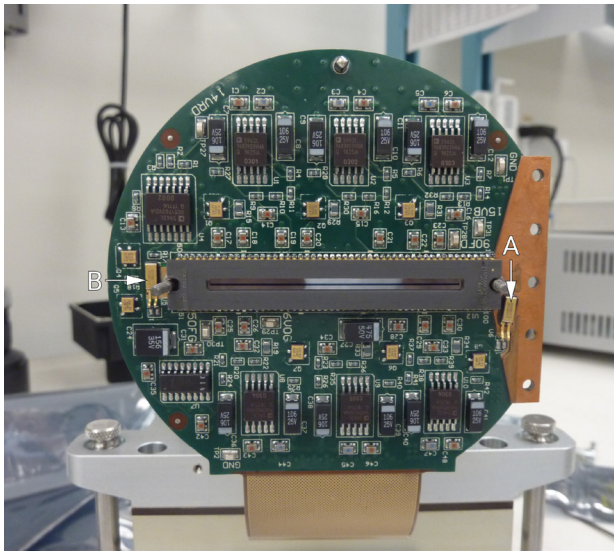


Fig. 8. ShadowCam flight focal plane printed circuit board. The TDI line array detector package, running horizontally across the middle of the board in this view, is 66 mm long. The narrow slit along the long axis of the detector package is the custom light shield aperture that exposes only 32 of the 128 lines (3.6" diameter). Arrows labeled A (label) and B (label) indicate temperature thermistors. TDI, time delay integration.

different from CTX and much larger in area, as it must implement the signal chain for twelve independent outputs, six each for the two TDI directions. Twelve operational amplifiers are used, with the two TDI directions of each CCD output multiplexed into one input of the two ADCs. The inactive TDI direction outputs are disabled to reduce power dissipation on the CCD die. The nominal system scale factor with the analog-front-end is set to a unity gain of 51.4 e-/DN, and the read noise is about 1 DN.

The remainder of the system is quite similar to CTX. More clock drivers of the same type are needed to drive all of the Hamamatsu sensor clocks, the low-voltage differential signaling (LVDS) interface drivers and receivers are replaced with RS-422 equivalents, and some voltage regulators are new to avoid obsolescence.

The electrical interface with the spacecraft is simple. A redundant RS-232 UART interface, running at 115,200 baud, is used for commanding. From the spacecraft perspective, commands are fixed-length and 70 bytes long; consisting of 35 16-bit commands with a 4-bit opcode and a 12-bit operand. Commands are provided to set the line rate, number of lines, DRAM base address, and metadata values for images, as well as to adjust the internal registers of the ADCs for gain and offset control, loading parameters for the companding logic, and starting image acquisition and readout. A single 70-byte command block can set all the needed parameters, start image acquisition, wait for it to complete, and then read the image data to the spacecraft. The timing

of the image start is entirely controlled by the spacecraft. The data interface is a synchronous parallel interface with a clock, a frame sync signal, and two data lines. This interface runs at 2 MHz, so reading out the entire DRAM buffer takes about 9 minutes. If desired, multiple smaller images can be commanded without read out, and then the whole buffer can be read out later, allowing more closely-spaced image timing.

ShadowCam includes six heaters for survival, operations, and bakeout of the composite structure (which would otherwise be out of focus due to water absorption). There are unique heaters for decontamination (driving water out of the composite structure prior to commencement of operations) and survival heat (extremely cold cases). There are redundant heaters to provide operational heat to maintain ShadowCam within allowable flight temperature (AFT) ranges on the optics tube and at the interface plate. Heaters are switched by the spacecraft and controlled with redundant hardware thermostats. Four AD590-type temperature sensors are read by the spacecraft to measure the FPA temperature (two sensors), the main electronics temperature, and the temperature of the optical metering structure (Fig. 7).

4.3 Thermal Control (Radiator, Blanketing, Decontamination Heater, Survival Heaters)

The ShadowCam thermal system (Fig. 9) leverages heavily on the heritage of the LROC NAC, which is thermally isolated from the spacecraft and deploys an aluminum radiator to reject heat to deep space. However, the NAC radiator has a continuous deep space view, due in part to the semi-annual yaw flip that the spacecraft performs to keep its solar arrays pointed at the sun (Beckman 2007), but also due to the LRO thermal design that provided clear space views for radiators at the expense of redoing mechanical design (Baker et al. 2009) enabling the LROC NAC to have a simple aluminum radiator with a large Sun-exclusion shroud and constant Sun-free, clear view of space. The KPLO spacecraft did not share the same design

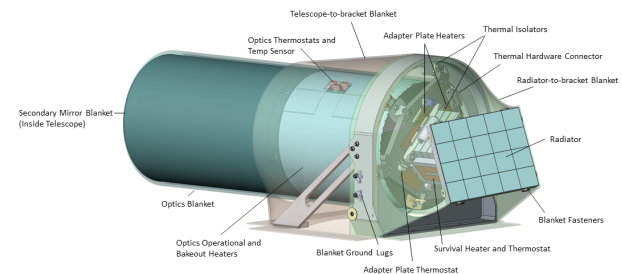


Fig. 9. ShadowCam Thermal Hardware.

philosophy, and the ShadowCam instrument was situated on a part of the spacecraft that lacked a clear space view and received direct solar illumination throughout the entire mission. This deployment position necessitated a different thermal rejection system. After performing numerous trades on radiator size, view factors, and emissive surface materials, it was determined that an Optical Solar Reflectors (OSRs) would meet requirements, due to the inherently low solar absorptance and high emissivity of the material.

While OSRs are used on almost every major spacecraft for thermal control of Sun-facing surfaces (<https://www.excelitas.com/product/optical-solar-reflectors>), MSSS had never built an instrument incorporating the technology. Therefore, design and manufacturing processes needed to be developed and qualified. A trade study was performed to select a means of attaching the OSRs to the radiator substrate. After a review of twelve adhesives, an electrically conductive, pressure-sensitive adhesive was chosen as it represented the best compromise between ease of use, adhesion, temperature range, outgassing, and flight heritage. To qualify the design, sample radiator panels were assembled and put through environmental testing to verify that the OSRs did not crack or disjoin (Fig. 10). The radiator panel was qualified to random vibration levels in Table 2.4-3 of GSFC-STD-7000A. The same unit was then cycled in a thermal vacuum over the predicted survival temperature range.

Six heater circuits are wired to a d-subminiature connector fastened to the adapter plate (Fig. 11, Table 3). Four circuits are redundant operational heaters on the telescope metering tube and the adapter plate. The telescope metering tube operational heaters keep the optics within operational temperature limits, whereas the adapter plate heaters prevent thermal distortion of the titanium adapter plate from imparting load on the optical bench through the telescope flexures. A survival heater is located on the

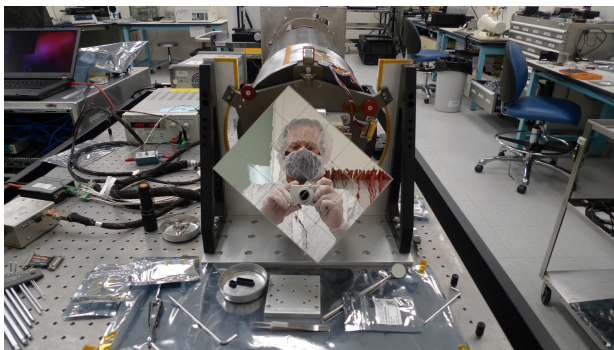


Fig. 10. The rear of the instrument with the emissive surface of the OSR radiator (flight unit) reflecting M. Clark of MSSS. OSR, Optical Solar Reflectors; MSSS, Malin Space Science Systems.

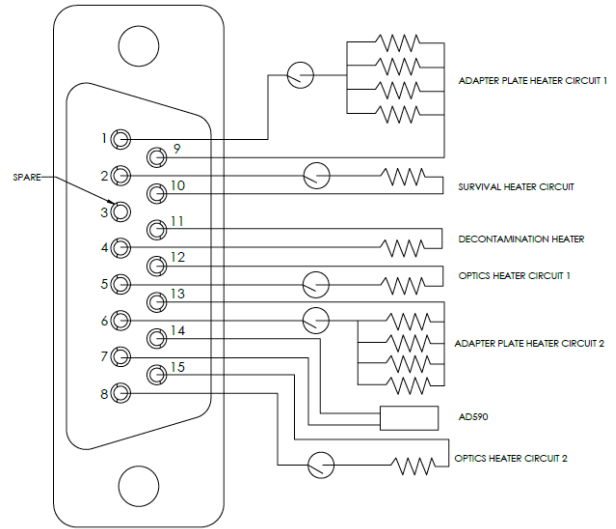


Fig. 11. ShadowCam Thermal Hardware Circuits.

Table 3. ShadowCam heater power and thermostat set-points

Heater	Power (W)	Thermostat range
Bakeout	32.0	N+58°C to +63°C
Survival	6.4	-45°C to -40°C
Optics operational primary	15.0	-32°C to -27°C
Optics operational secondary	15.0	-32°C to -27°C
Adapter plate primary	16.0	-3.3°C to 3.3°C
Adapter plate secondary	16.0	-3.3°C to 3.3°C

side of the radiator that is powered during eclipses to counteract the heat rejection of the radiator, keeping the electronics within their survival temperature range. Finally, a decontamination heater (or bakeout heater) is collocated with the telescope operational heaters, allowing moisture to be baked out of the hygroscopic carbon fiber-reinforced polymers (CFRP) metering tube.

G10 thermal isolators are implemented at the spacecraft mounting interface, between the adapter plate and the spacecraft mounting bracket, acting as an isolator for the entire instrument. Additionally, isolators are used between the electronics assembly and adapter plate to prevent heat transfer between the adapter plate heaters and electronics.

All surfaces of the instrument were blanketed except for the telescope aperture and radiator emissive surface. Inside the telescope, the scene-facing side of the secondary mirror was blanketed to prevent IR from the lunar surface from heating the optical structure. A black Kapton outer layer was used for stray light mitigation. Another blanket is wrapped around the telescope sunshade and metering tube and affixed with pressure-sensitive adhesive. Two blankets cover the spacecraft mounting bracket, electronics, and

telescope metering tube. One blanket is affixed around the perimeter of the radiator with pressure-sensitive adhesive and fastened with ultem blanket standoffs. That blanket is fastened to the spacecraft bracket and taped to the optics tube blanket, which spans between the bracket and telescope metering tube (effectively giving the metering tube two blankets). Fabricating these blankets was unusually difficult given that they were being built during the height of the Covid-19 pandemic. While blankets would typically be built up with the flight hardware and spacecraft, that was not an option due to international pandemic protocols. Given that the blankets were fabricated not only interface to the instrument, but also portions of the spacecraft, and that sending a technician to Korea Aerospace Research Institute (KARI) to modify blankets was not feasible, a high-fidelity model was built of both the spacecraft and instrument to ensure that the blankets would fit without modification when shipped to KARI and installed by KARI technicians. The ShadowCam blankets (Fig. 12) were designed and fabricated by Destiny Support in College Park, MD.

To keep the sensor below room temperature to limit dark current, several features were added to the electronics to minimize the temperature of the focal plane (Fig. 13). Because the sensor is mounting directly to the telescope and weakly coupled to the radiator via a rigid-flex section of the circuit board, heat straps were designed to couple the focal plane to the radiator directly. Given the very limited access to the heritage hardware, a forming fixture was designed to give the heat straps a specific shape and length. The heat straps were fabricated out of copper braid, such that load from the electronics would not be transferred to the focal plane, given the flexures in the structural load path between the telescope and adapter plate. Because the only access point for the heat straps was to the edge of the detector,



Fig. 12. ShadowCam instrument undergoing flight blanket fit-check.

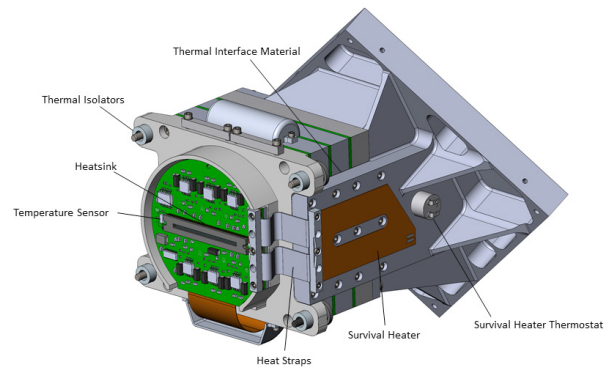


Fig. 13. Electronics thermal hardware.

a copper heat sink was bonded between the sensor and PCB and directly coupled to the heat strap to decrease the thermal gradient across the detector (Fig. 8). Temperature sensors on either side of the detector are soldered to the circuit board to monitor temperature across the detector although it should be noted that the sensor further from the heat strap has a thermal lag.

4.4 Structural Design

The primary structure of the ShadowCam instrument is the adapter plate; a Titanium 6Al-4 V plate that provides the spacecraft mounting interface and interfaces between the electronics and telescope. The adapter plate remained largely unchanged from the LROC NAC cameras besides the addition of inserts for alignment cubes and connectors and because it serves as the foundation of the telescope. To prevent loading into the optical bench that would be imparted by dimensional differences between the adapter plate and telescope flexures, the Titanium 6Al-4 V flexures were installed on the adapter plate and match bonded to the optical bench. This configuration provides a zero-stress connection between the adapter plate and the telescope optical bench.

The optical bench is an egg-crate CFRP sandwich panel to which the primary mirror and corrector optics are bonded. Invar inserts are bonded in the optical bench to serve as an attachment point for the metering tube. The metering tube is a carbon fiber composite that employs unidirectional plies oriented in a thermally stable, quasi-isotropic orientation with a cyanate ester matrix. The tube is reinforced with a series of longerons, to which the secondary mirror is attached. Fittings are bonded between the longerons to serve as an attachment point for the stray light mitigation baffle. The stray light mitigation baffle is a CFRP tube with 15 baffle vanes (Fig. 14), an improvement over the 5-vane

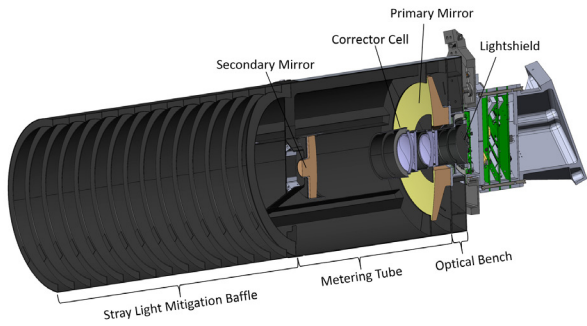


Fig. 14. Telescope structural components.

LROC design.

The electronics are bolted to the adapter plate via G10 thermal isolators. The rigid-flex circuit board is clamped between 6061-T6 aluminum housings. The radiator bolts to the back of the electronics and along the side of the electronics to reject heat. The focal plane board is bolted to the telescope with a focus spacer and light shield between the two assemblies. The ShadowCam sensor differs from the heritage LROC and CTX instruments and requires a larger board size. Since the sensor is bolted to the telescope and supports the larger focal plane board, testing was performed to ensure the sensor package could handle random vibration loads. A conservative static load of 12.4 lbs. was derived from the analytical response of the board during random vibration. A static load fixture was designed, and the mass was successfully hung off the sensor mounting points (Figs. 15, 16).

A more pressing structural concern in random vibration was the bonded rib attached to the secondary mirror. During random vibration testing of the LROC instruments, the secondary mirror was instrumented with an accelerometer that showed minimal damping in the composite structure. This accelerometer data led to relatively deep notches being applied to the random vibration profile at the resonant

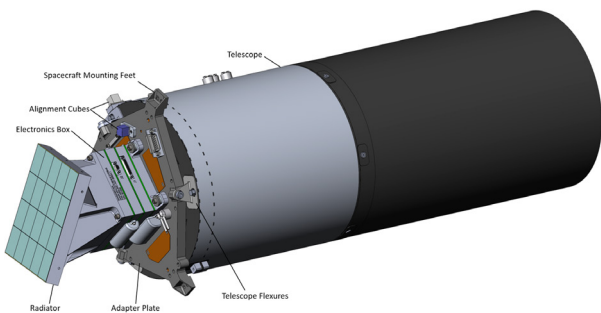


Fig. 15. ShadowCam Instrument Structural Components.

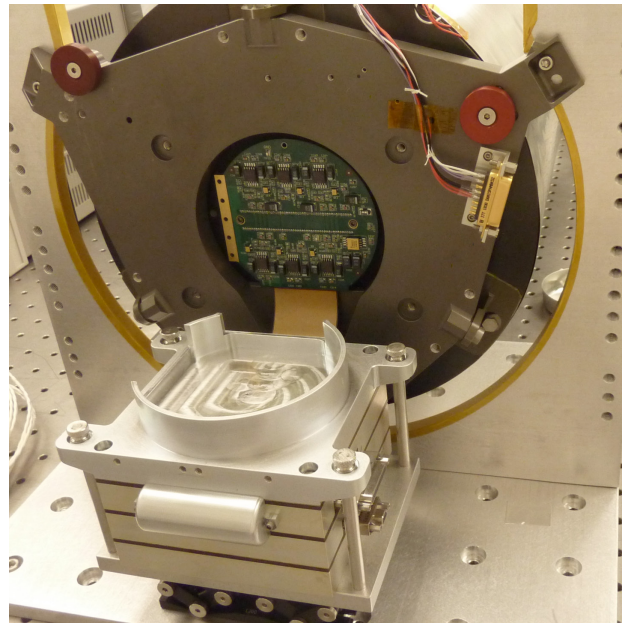


Fig. 16. Round FPA board (sensor on the other side) bolted to the back of the telescope, connected to the rest of the electronics assembly via the flex cable seen at the bottom of the board. The aluminum electronics assembly was rotated upwards 90 degrees against the FPA board in the final assembly. FPA, focal Plane Assembly.

frequencies of the secondary mirror structure. The KPLO spacecraft configuration would not allow for such deep profile notches, and a considerable amount of effort was expended to ensure the instrument would survive launch. First, the ShadowCam spacecraft bracket was instrumented with accelerometers during the KPLO spacecraft mockup acoustic test. The responses from these accelerometers were enveloped to generate a new, more benign random vibration profile. However, this profile stipulated that no notching could be applied. This required reinforcement to the instrument structure applied relatively late in the build.

The LROC telescope Finite Element Model (FEM) was tuned with the damping coefficients determined during the LROC random vibration test to determine what reinforcements were necessary. Additionally, the FEM was updated with higher fidelity to model the bonded carbon fiber structure better. This high-fidelity model, when run with the latest random vibration spectra, showed the lap bond between the secondary mirror structure and metering tube failing when loaded in the boresight direction.

To better define the bonded joint allowables, additional test specimens were fabricated. The T-joint and H-joint test coupons were assembled and tested to add fidelity to the telescope bond allowables (Fig. 17). While that data was helpful, it was not enough to show a positive margin in the telescope bonds.

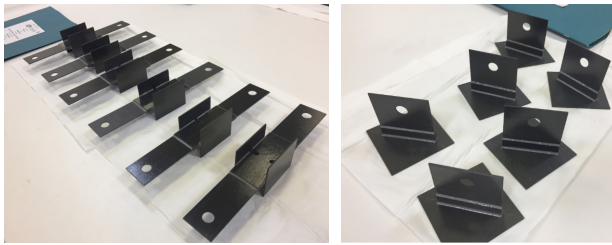


Fig. 17. Test coupons fabricated for generating bonded joint allowables.

Given that the telescope structure had already been fabricated, changes to the structure needed to be added without redesigning the assembly. Doublers were designed for the secondary mirror lap bonds, creating a double lap bond at this critical joint that could show positive margin with the KPLO vibration levels. The telescope structure was reworked to include this doubler prior to installing optical components.

The ShadowCam instrument was tested to proto-flight random vibration levels at National Technical Systems in Los Angeles, CA. Accelerometers were installed on the secondary mirror, the electronics box, and the adapter plate. The test went smoothly, with pre/post-test signatures showing virtually no frequency or amplitude shift. Post-test imaging with the instrument confirmed that ShadowCam successfully passed the random vibration test and was ready to proceed with the environmental test campaign (Fig. 18).

4.5 Radiation Shielding and Analysis

The radiation shielding methodology for ShadowCam is primarily based on the heritage of the LROC NAC. The electronics box housings are 0.100-inch thick aluminum. The Focal Plane has additional shielding on the back side of .300 inches of aluminum. We performed a sector analysis to estimate the expected dose throughout the mission. The CAD model was cross-sectioned and split into rays to complete the sector analysis. The total aluminum-equivalent shielding was calculated along each ray, and the KPLO-supplied dose-depth table was used to determine the correlating dose. The total mission dose was determined by summing each ray. Sector analysis was performed at the sensor location (Total Ionizing Dose, TID, and Dose Displacement Damage, DDD) and the center of the electronics stack (Total Ionizing Dose only). The results of the sector analysis were 1.381 krad(si) TID and $2.59E + 07$ MeV/g(si) DDD over the mission lifetime. We estimated the electronics box would receive 4.549 krad(si) TID over the mission lifetime.



Fig. 18. R. Dahl-Hansen installing the ShadowCam instrument on the random vibration shaker for Z-axis testing.

4.6 Environmental Testing

Testing on the flight hardware began at the Printed Circuit Board level. The board was thermally cycled and burned in for 500 hours. The unit was subjected to random vibration testing at the integrated instrument level. Random vibration loads were generated by KARI using data from an acoustic test on a flight-like spacecraft model. The unit was hard-mounted to the shaker without force limiting, and the duration was 1min/axis. The unit was instrumented with three accelerometers on the secondary mirror, electronics box, and adapter plate. We ran low-level random signature surveys before and after the 0-dB run for each axis to identify problematic frequency or amplitude shifts, none of which were observed. After successful random vibration testing, thermal vacuum testing was performed in the MSSS thermal vacuum chamber. The goal of the thermal vacuum test was to verify the functionality of the thermal control system (radiator, heaters, and blanketing), bake out the flight hardware to remove volatile contaminants, verify the functionality of the instrument at proto-flight temperature extremes, and verify the unit survives extreme non-operating proto-flight temperatures. Five thermal cycles

were performed, and thermal balance data was obtained over various environment temperatures and operational modes. We designed and fabricated a liquid nitrogen-cooled plate to test radiator functionality. The plate was placed directly before the radiator to simulate a space view. The aperture of the instrument pointed out a window in the thermal vacuum chamber and imaged a collimator with a test target at infinite conjugate (Fig. 4).

We performed EMI/EMC testing on a non-flight version of the electronics, including Conducted Emissions, Conducted Susceptibility (CS114), Radiated Emissions (RE101), and Radiated Susceptibility (RS03). A test fixture was assembled to perform proton dose testing of unbiased sensor samples to determine end-of-life displacement damage dose effects at 1x and 2x the expected shielded dose.

5. CONCEPT OF OPERATIONS

Due to downlink restrictions, the original concept of operations for ShadowCam was to acquire targeted partial images of only permanently shadowed areas near the poles with areas greater than 10 km^2 (within 9° latitude of each pole); however, there was some uncertainty about the predict ephemeris accuracy. With the KPLO ground speed of $\sim 1.6 \text{ km/s}$, a 1-second timing uncertainty would result in a $\sim 1,000$ line shift in the resulting ShadowCam image. If a PSR were only 6 km along-track, a 1,000 line error would result in only partial coverage of that PSR. This targeted approach required lengthening images on either side of a PSR to account for predict uncertainty, and this buffer would significantly increase the downlink volume

KARI and NASA agreed in the Spring of 2020 to increase the downlink capabilities of KPLO by adding four X-band downlink passes each day for a total of eight contacts per day (four via the KARI Deep Space Antenna and four with the NASA Deep Space Network). These additional passes increased the science data downlink to as much as $\sim 149 \text{ Gib/day}$ (shared among the entire spacecraft and instruments).

With this additional downlink, we revised the concept of operations to use a collar image strategy that greatly reduces the impact of predict uncertainties and simplifies target planning (Fig. 19). Additionally, the collar strategy accumulates coverage of PSRs of all sizes and temporarily shadowed areas in all areas that would otherwise be missed by the targeted approach getting only PSRs $> 10 \text{ km}$ in size.

In its simplest form, the collar strategy builds up complete coverage of a polar region (within 9° latitude of the pole) over three months. The middle of the three-month period is

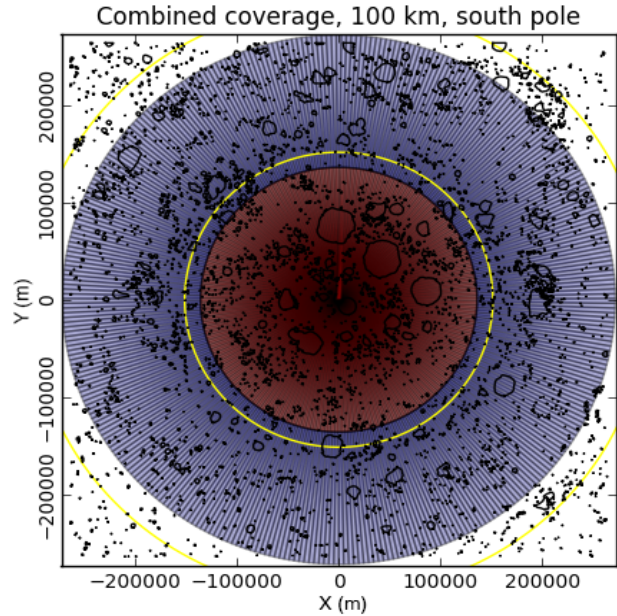


Fig. 19. Collar strategy after two months, inner (red) and outer (blue). Footprints were computed assuming a fixed 100 km altitude and 90° inclination. The inner yellow circle corresponds to the 85°S latitude, and the outer yellow circle corresponds to the 80°S latitude.

placed at the summer solstice. Six weeks before the solstice, ShadowCam acquires a collar that covers 81° to 85.7° through a full 360° of longitude. Four weeks later, the collar is shifted towards the pole and then covers 85.5° to 0.2° beyond the pole. After eight weeks, ShadowCam acquires a second outer collar, ensuring that low latitude gaps are covered and providing short time-based temporal coverage.

In practice, the acquired collars vary in footprint size, orientation, start and end points, and pixel scale relative to the ideal case described above due to variations in altitude (± 20 kilometers) and orbital inclination ($\pm 0.5^\circ$).

This increased downlink budget allows ShadowCam to acquire a full buffer image at each pole during every orbit, plus an additional six images (1,536 MiB) allocated daily for calibration and equatorial imaging. Due to power constraints, there is a small window near Solar Beta 45° where the spacecraft must be slewed off nadir, which may reduce the available downlink and thus reduce the total number of observations ShadowCam can collect (impacting 1-2 orbits).

Secondary lighting within a PSR depends on the location of the PSR, the distance from the directly illuminated surrounding topography, and the local topography within a PSR. Seasonality in lighting corresponds to the subsolar latitude (brighter south pole PSRs at south pole summer – subsolar latitude $< 0^\circ$), and subsolar longitude variations illustrate topographic dependence (Fig. 20). Direct illumination maximum, i.e., “noon” primary lighting, may

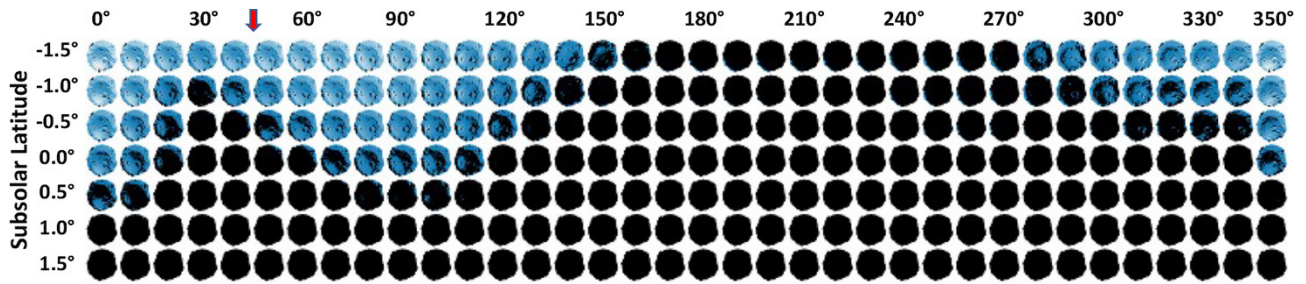


Fig. 20. Seasonal lighting within Shoemaker crater (88.026°S, 45.279°E) as a function of sub-solar latitude and longitude. The red arrow shows the local noon lighting. Lighting is poor at sub-solar longitudes between 150° to 280°, even during summer.

not produce the best secondary lighting inside the PSR. When combined with the positioning of the KPLO orbit such that ShadowCam can acquire an image at the best lighting condition, multiple observations spanning multiple mission months can be required to build up a complete mosaic of a PSR with all parts having optimal S/N (Fig. 21). For example, if the equator-facing interior wall is lower than the eastern interior wall, there will be less secondary illumination at noon; the Sun is slightly higher above the horizon, and the reflection area is significantly decreased relative to the morning. Local and distant topography can occlude incoming reflected illumination, reducing the lighting within the PSR.

Because the principles of TDI sensing rely on each successive row of pixels imaging the same feature in each

time step, the line exposure time (line time) for an image needs to be synchronized to the ground speed and pixel scale of the spacecraft during that image (Speyerer et al. 2023). Pixel scale is a function of the distance between the spacecraft and the surface, which varies with both orbital radius and ground elevation. Because ShadowCam has a fixed line time for each image, it effectively has a limited depth of field: Terrain that is > 3 km from the targeted distance will have > 1 pixel of smear from ground speed/line time mismatch. This relation results in smearing within portions of large deep craters, or when a large deep crater is adjacent to a towering massif.

Our strategy for choosing an optimal line time for each image is to calculate the ideal line time for each indirectly illuminated pixel within the planned image area. We calculate the line time using the predicted ephemeris for orbit position and velocity and a global DTM depicting surface topography. Line rates are calculated for each 100 m square bin within the footprint, and the median line rate is selected. The same tool can present a smear map to the operations team showing the ideal line rate for each 100 m bin in the scene, so if the science team needs to minimize smear on a particular landform, this information is available. Smear effects across the whole image footprint are presented graphically to the operations team. This same line rate tool is used later with the definitive ephemeris to produce a smear map released to Planetary Data System (PDS) to help interpret the resulting data.

When smearing is expected because the distance to the ground within an image changes too much, we split an image into two or more smaller segments with different line times, optimized for each region (Fig. 22). However, as ShadowCam requires a minimum 1-second gap between the end of one image and the start of the next, there is at least a 3.4 km gap between the sub-images. When possible, this gap is positioned to primarily cover terrain that is expected to be fully illuminated (and thus saturated).

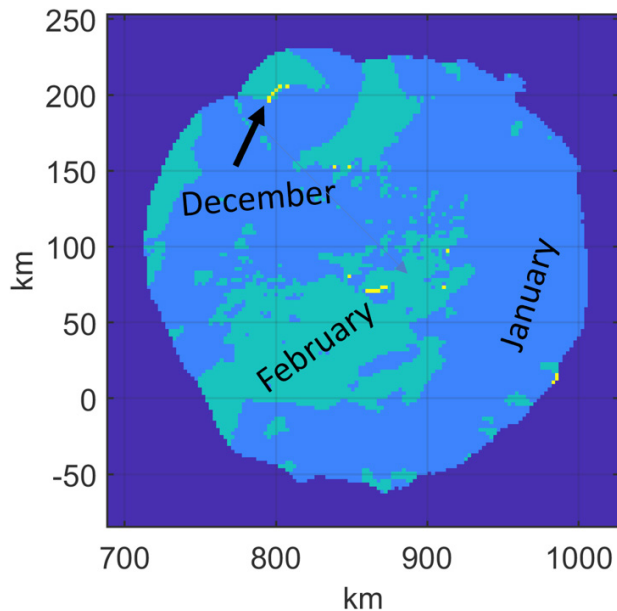


Fig. 21. ShadowCam nominal mission months (2023) when secondary illumination irradiance is maximum inside the Faustini PSR. Planning and imaging over multiple months is required to acquire the best signal-to-noise ratio over the entire PSR. PSR, permanently shadowed regions.

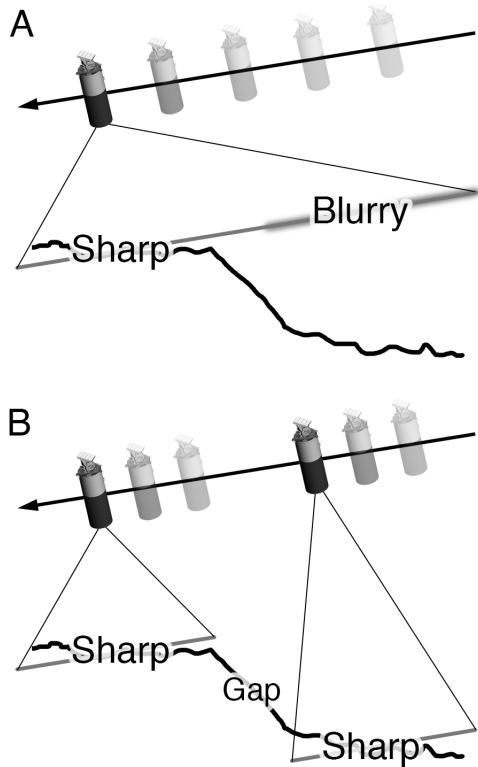


Fig. 22. Splitting an image to remove smearing. (A) A single image covering terrain with > 3 km distance to the target due to a combination of spacecraft altitude and ground elevation. The line rate is optimized for the higher elevation, so the lower elevation region is smeared (blurry). (B) Same location with coverage split into two sub-images; both are sharp, but there is a coverage gap between them.

6. GROUND DATA SYSTEM

The Science Operations Center (SOC) ground data system handles all target planning, processing, cataloging, archiving, and other automated processes coordinated by a central database (Fig. 23). Data transfer to and from the KARI MOC uses the SOC Data Exchange System (DES) and the KARI-deployed External Data Server (EDS). EDS hosts the data server for both directions, and DES pulls data from EDS and pushes the SOC data back to EDS over a secure connection. The flow of operations starts with KARI sending predict kernels to the SOC. Then, JMoon (a derivative of the JMARS software, JMARS, Arizona State University, Tempe, AZ; Christensen et al. 2009) and other targeting tools are used to create a target plan with input from the ShadowCam science team. After constraint checking, daily command sequences are sent to KARI via DES. KARI integrates the commands with the other spacecraft activity and sends the sequence to KPLO. As ShadowCam acquires images, they are stored on the KPLO payload data handling unit (PDHU). During the eight downlink passes each day, data is transferred from the PDHU to the ground and removed from the PDHU to free space for the next set of images. Once on the ground, KARI sends the instrument files, definitive SPICE (Acton 1996), and housekeeping data to the SOC. The SOC uses the Rector job management software developed in-house to support LROC in cataloging and processing this data into various products, including raw and calibrated PDS products, smear

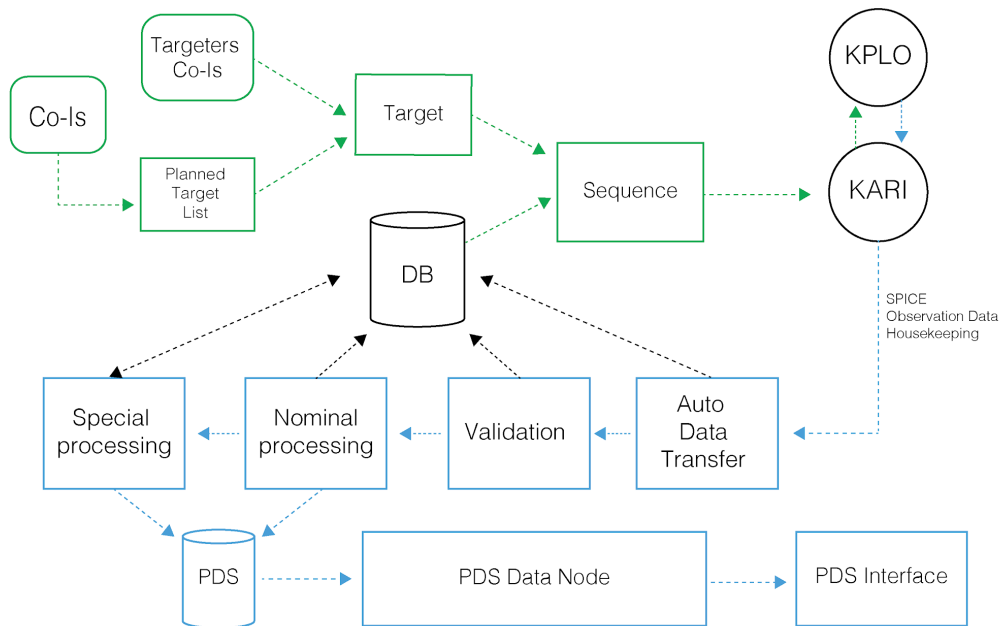


Fig. 23. ShadowCam operations flow diagram. KPLO, Korea Path-finder Lunar Orbiter; KARI, Korea Aerospace Research Institute; PDS, Planetary Data System.

maps, and ancillary support data such as browse images (Estes et al. 2012). This data is all made available in the SOC's data portal alongside all other data managed by the SOC. This strategy allows the science team to search and access all of the lunar data sets in the SOC in a single interface, and published data sets are available for the public in this same tool. The data portal leverages the LROC SOC-developed Lunaserv to provide the map data via the web map service (WMS) standard using the correct Moon spatial reference systems (Estes et al. 2013) along with a comprehensive text search originally developed by LROC SOC developers as the International Space Station Instrument Integration Implementation (I4) tool (Stefanov et al. 2015).

The ShadowCam team will include software to process raw ShadowCam observations to radiometrically calibrate and map project images within the United States Geological Survey Integrated Software for Imaging Spectrometers.

7. CONCLUSIONS

The ShadowCam instrument is performing nominally and has met or exceeded all performance requirements (Humm et al. 2023). The instrument can image within the expected radiance range of 0.01 to 0.56 W/m²/sr/um (dependent on altitude, which controls line time) with a S/N of 100 at 0.12 W/m²/sr/um. Surface detail can be seen in images with radiances as low as 0.006, allowing regions illuminated under earthshine to be imaged.

The MTF (Humm et al. 2023) has a direct bearing on image sharpness, together with jitter and motion smear; inspection of the returned images gives a positive measure of the overall sharpness and resolving capability of the instrument (Fig. 24).

After the nominal mission is completed, analysts will be able to retire the ShadowCam science objectives and goals.

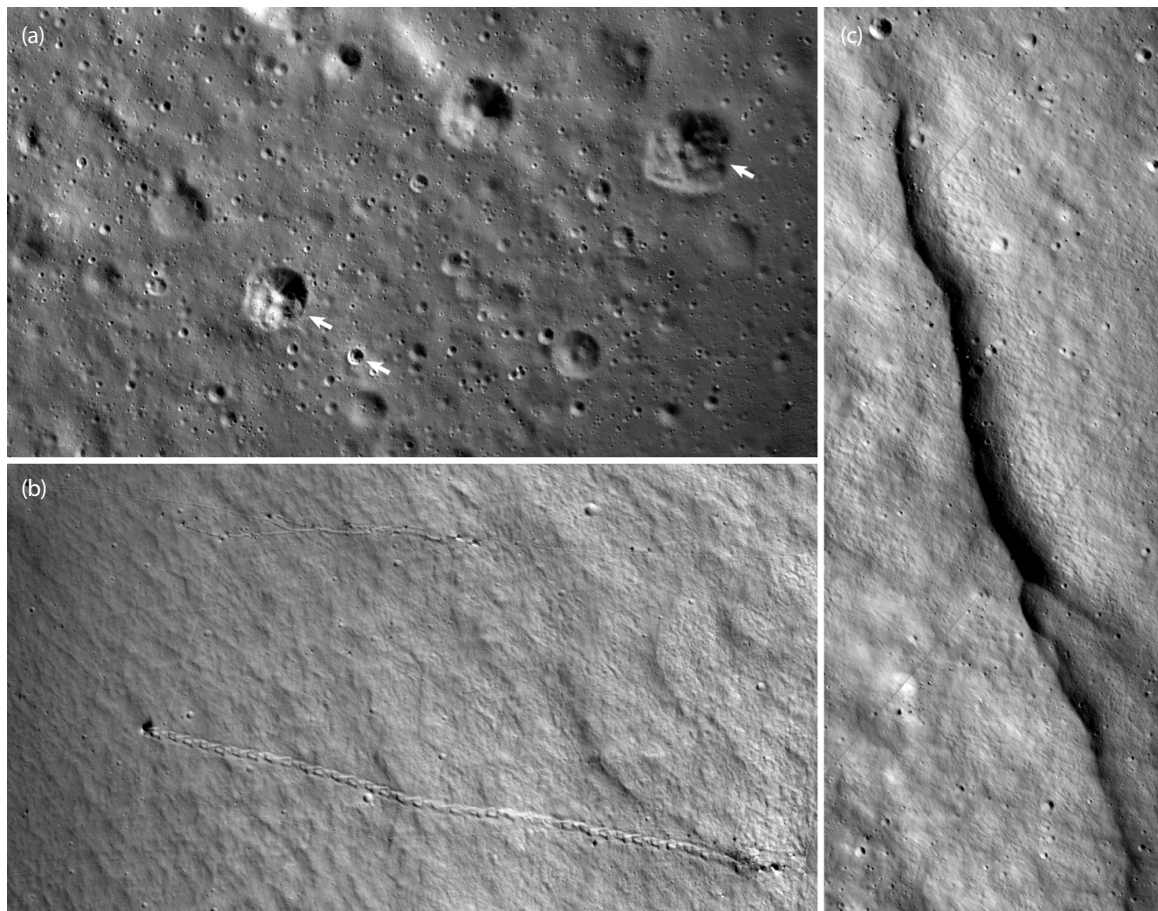


Fig. 24. Examples of landforms in PSRs imaged by ShadowCam. (a) Floor of Hermite A crater with irregular floor craters (arrows). Note the distinctive reflectance pattern in the smallest arrowed crater, image 2,520 meters wide, centered at 88.013°N, 311.08°E, ShadowCam M029254247. (b) Boulder trails on wall of Plaskett U crater; boulder at base of widest trail is ~25 meters across, image 2,520 meters wide, centered at 82.399°N, 161.48°E, ShadowCam M014845598. (c) Lobate scarp within Mouchez L crater, 1,060 meters wide, centered at 78.585°N, 318.79°E, ShadowCam M013852543. PSR, permanently shadowed regions.

ACKNOWLEDGMENTS

We thank the many contractors who helped realize ShadowCam, John Guidi (NASA) and Chris Zavrel (NASA) for wise and efficient project oversight, and the KARI team for carrying us to the Moon on the amazing Danuri lunar orbiter.

ORCID*s*

Mark Southwick Robinson
<https://orcid.org/0000-0001-9964-2932>
 Scott Michael Brylow
<https://orcid.org/0009-0008-9398-2723>
 Michael Alan Caplinger
<https://orcid.org/0009-0005-1707-9004>
 Lynn Marie Carter
<https://orcid.org/0000-0002-6245-4142>
 Matthew John Clark
<https://orcid.org/0009-0007-8985-8546>
 Brett Wilcox Denevi
<https://orcid.org/0000-0001-7837-6663>
 Nicholas Michael Estes
<https://orcid.org/0009-0008-3576-8366>
 David Carl Humm
<https://orcid.org/0000-0003-1520-261X>
 Prasun Mahanti
<https://orcid.org/0000-0003-0805-8074>
 Douglas Arden Peckham
<https://orcid.org/0009-0000-2347-4055>
 Michael Andrew Ravine
<https://orcid.org/0000-0003-4810-7352>
 Jacob Andrieu Schaffner
<http://orcid.org/0000-0001-9885-5346>
 Emerson Jacob Speyerer
<https://orcid.org/0000-0001-9354-1858>
 Robert Vernon Wagner
<https://orcid.org/0000-0001-5999-0721>

REFERENCES

- Acton CH Jr, Ancillary data services of NASA's navigation and ancillary information facility, *Planet. Space Sci.* 44, 65-70 (1996). [https://doi.org/10.1016/0032-0633\(95\)00107-7](https://doi.org/10.1016/0032-0633(95)00107-7)
- Arnold JR, Ice in the lunar polar regions, *J. Geophys. Res. Solid Earth.* 84, 5659-5668 (1979). <https://doi.org/10.1029/JB084iB10p05659>
- Baker C, Cottingham C, Garrison M, Melak T, Peabody S, et al., Lunar Reconnaissance Orbiter (LRO) rapid thermal design development, in *Heatpipes for Space Applications International Conference, Moscow, 15-18 Sep 2009.*
- Barker MK, Mazarico E, Neumann GA, Smith DE, Zuber MT, et al., Improved LOLA elevation maps for south pole landing sites: error estimates and their impact on illumination conditions, *Planet. Space Sci.* 203, 105119 (2021). <https://doi.org/10.1016/j.pss.2020.105119>
- Beckman M, Mission design for the Lunar Reconnaissance Orbiter, in *29th Annual Advances in the Astronautical Sciences Guidance and Control Conference, Breckenridge, CO, USA, 4-8 Feb 2007.*
- Beyer R, Alexandrov O, Balaban E, Colaprete A, Shirley M, et al., VIPER geospatial data for site selection and traverse planning, *LPI Contrib.* 2806, 2377 (2023).
- Bickel VT, Kring DA, Lunar south pole boulders and boulder tracks: implications for crew and rover traverses, *Icarus* 348, 113850 (2020). <https://doi.org/10.1016/j.icarus.2020.113850>
- Boynton WV, Droege GF, Mitrofanov IG, McClanahan TP, Sanin AB, et al., High spatial resolution studies of epithermal neutron emission from the lunar poles: constraints on hydrogen mobility, *J. Geophys. Res. Planets* 117, E00H33 (2012). <https://doi.org/10.1029/2011JE003979>
- Braden SE, Robinson MS, Relative rates of optical maturation of regolith on Mercury and the Moon, *J. Geophys. Res. Planets* 118, 1903-1914 (2013). <https://doi.org/10.1002/jgre.20143>
- Brown HM, Boyd AK, Denevi BW, Henriksen MR, Manheim MR, et al., Resource potential of lunar permanently shadowed regions, *Icarus* 377, 114874 (2022). <https://doi.org/10.1016/j.icarus.2021.114874>
- Bussey DBJ, Lucey PG, Steutel D, Robinson MS, Spudis PD, et al., Permanent shadow in simple craters near the lunar poles, *Geophys. Res. Lett.* 30, 1278 (2003). <https://doi.org/10.1029/2002GL016180>
- Bussey DBJ, McGovern JA, Spudis PD, Neish CD, Noda H, et al., Illumination conditions of the south pole of the Moon derived using Kaguya topography, *Icarus* 208, 558-564 (2010). <https://doi.org/10.1016/j.icarus.2010.03.028>
- Bussey DBJ, Spudis PD, Robinson MS, Illumination conditions at the lunar south pole, *Geophys. Res. Lett.* 26, 1187-1190 (1999). <https://doi.org/10.1029/1999GL900213>
- Campbell BA, High circular polarization ratios in radar scattering from geologic targets, *J. Geophys. Res. Planets* 117, E06008 (2012). <https://doi.org/10.1029/2012JE004061>
- Campbell DB, Campbell BA, Carter LM, Margot JL, Stacy NJS, No evidence for thick deposits of ice at the lunar south pole, *Nature* 443, 835-837 (2006). <https://doi.org/10.1038/nature05167>
- Chabot NL, Ernst CM, Denevi BW, Nair H, Deutsch AN, et al., Images of surface volatiles in Mercury's polar craters acquired by the MESSENGER spacecraft, *Geology.* 42, 1051-1054 (2014). <https://doi.org/10.1130/G35916.1>

- Chabot NL, Ernst CM, Paige DA, Nair H, Denevi BW, et al., Imaging Mercury's polar deposits during MESSENGER's low-altitude campaign, *Geophys. Res. Lett.* 43, 9461-9468 (2016). <https://doi.org/10.1002/2016GL070403>
- Chowdhury AR, Saxena M, Kumar A, Joshi SR, Amitabh, et al., Orbiter high resolution camera onboard Chandrayaan-2 orbiter, *Curr. Sci.* 117, 560-565 (2019). <https://doi.org/10.18520/cs/v118/i4/560-565>
- Christensen PR, Engle E, Anwar S, Dickenshied S, Noss D, et al., JMARS – a planetary GIS, in American Geophysical Union, Fall Meeting 2009, San Francisco, CA, 14-18 Dec 2009.
- Cintala MJ, McBride KM, Block distribution on the lunar surface: a comparison between measurements obtained from surface and orbital photography, NASA Technical Memorandum #104804 (NASA Johnson Space Center, Houston, 1995) 41.
- Clark RN, Detection of adsorbed water and hydroxyl on the Moon, *Science* 326, 562-564 (2009). <https://doi.org/10.1126/science.1178105>
- Colaprete A, Schultz P, Heldmann J, Wooden D, Shirley M, et al., Detection of water in the LCROSS ejecta plume, *Science* 330, 463-468 (2010). <https://doi.org/10.1126/science.1186986>
- Dagar AK, Rajasekhar RP, Nagori R, Analysis of the permanently shadowed region of Cabeus crater in lunar south pole using orbiter high resolution camera imagery, *Icarus* 406, 115762 (2023). <https://doi.org/10.1016/j.icarus.2023.115762>
- De Rosa D, Bussey B, Cahill JT, Lutz T, Crawford IA, et al., Characterisation of potential landing sites for the European Space Agency's Lunar Lander project, *Planet. Space Sci.* 74, 224-246 (2012). <https://doi.org/10.1016/j.pss.2012.08.002>
- Deutsch AN, Head JW, Parman SW, Wilson L, Neumann GA, et al., Degassing of volcanic extrusives on Mercury: potential contributions to transient atmospheres and buried polar deposits, *Earth Planet. Sci. Lett.* 564, 116907 (2021). <https://doi.org/10.1016/j.epsl.2021.116907>
- Dundas CM, Byrne S, McEwen AS, Mellon MT, Kennedy MR, et al., HiRISE observations of new impact craters exposing Martian ground ice, *J. Geophys. Res. Planets* 119, 109-127 (2014). <https://doi.org/10.1002/2013JE004482>
- Elphic RC, Eke VR, Teodoro LFA, Lawrence DJ, Bussey DBJ, Models of the distribution and abundance of hydrogen at the lunar south pole, *Geophys. Res. Lett.* 34, L13204 (2007). <https://doi.org/10.1029/2007GL029954>
- Estes NM, Hanger CD, Licht AA, Bowman-Cisneros E, Lunaserv Web Map Service: history, implementation details, development, and uses, in 44th Lunar and Planetary Science Conference, The Woodlands, TX, 18-22 Mar 2013.
- Estes NM, Bowley K, Paris K, Bowman-Cisneros, E, High performance computing with Rector: implementation, operation, and development, in Planetary Data Workshop, Flagstaff, AZ, 25-29 Jun 2012.
- Feder J, NASA prepares to drill for the “Oil of Space”, *J. Pet. Technol.* 73, 24-28 (2021). <https://doi.org/10.2118/0421-0024-jpt>
- Feldman WC, Maurice S, Binder AB, Barraclough BL, Elphic RC, et al., Fluxes of fast and epithermal neutrons from Lunar Prospector: evidence for water ice at the lunar poles, *Science* 281, 1496-1500 (1998). <https://doi.org/10.1126/science.281.5382.1496>
- Feldman WC, Lawrence DJ, Elphic RC, Barraclough BL, Maurice S, et al., Polar hydrogen deposits on the Moon, *J. Geophys. Res. Planets* 105, 4175-4195 (2000). <https://doi.org/10.1029/1999JE001129>
- Feldman WC, Maurice S, Lawrence DJ, Little RC, Lawson SL, et al., Evidence for water ice near the lunar poles, *J. Geophys. Res. Planets* 106, 23231-23251 (2001). <https://doi.org/10.1029/2000JE001444>
- Figuera RM, Riedel C, Rossi AP, Unnithan V, Depth to diameter analysis on small simple craters at the lunar south pole—possible implications for ice harboring, *Remote Sens.* 14, 450 (2022). <https://doi.org/10.3390/rs14030450>
- Fisher EA, Lucey PG, Lemelin M, Greenhagen B, Siegler M, et al., Search for lunar volatiles using the lunar orbiter laser altimeter and the diviner lunar radiometer, in 47th Lunar and Planetary Science Conference, The Woodlands, TX, 21-25 March 2016.
- Gladstone GR, Retherford KD, Egan AF, Kaufmann DE, Miles PF, et al., Far-ultraviolet reflectance properties of the Moon's permanently shadowed regions, *J. Geophys. Res. Planets* 117, E00H04 (2012). <https://doi.org/10.1029/2011JE003913>
- Gläser P, Haase I, Oberst J, Neumann GA, Co-registration of laser altimeter tracks with digital terrain models and applications in planetary science, *Planet. Space Sci.* 89, 111-117 (2013). <https://doi.org/10.1016/j.pss.2013.09.012>
- Gläser P, Sanin A, Williams JP, Mitrofanov I, Oberst J, Temperatures near the lunar poles and their correlation with hydrogen predicted by LEND, *J. Geophys. Res. Planets* 126, e2020JE006598 (2021). <https://doi.org/10.1029/2020JE006598>
- Gläser P, Scholten F, De Rosa D, Marco Figuera R, Oberst J, et al., Illumination conditions at the lunar south pole using high resolution digital terrain models from LOLA, *Icarus* 243, 78-90 (2014). <https://doi.org/10.1016/j.icarus.2014.08.013>
- Grier JA, McEwen AS, Lucey PG, Milazzo M, Strom RG, Optical maturity of ejecta from large rayed lunar craters, *J. Geophys. Res. Planets* 106, 32847-32862 (2001). <https://doi.org/10.1029/1999JE001160>
- Hapke B, Space weathering from Mercury to the asteroid belt, *J. Geophys. Res. Planets* 106, 10039-10073 (2001). <https://doi.org/10.1029/2000JE001338>
- Hapke B, Theory of Reflectance and Emittance Spectroscopy

- (Cambridge University Press, Cambridge, England, 2012).
- Harmon JK, Slade MA, Radar mapping of Mercury: full-disk images and polar anomalies, *Science* 258, 640-643 (1992). <https://doi.org/10.1126/science.258.5082.640>
- Harmon JK, Slade MA, Rice MS, Radar imagery of Mercury's putative polar ice: 1999–2005 Arecibo results, *Icarus* 211, 37-50 (2011). <https://doi.org/10.1016/j.icarus.2010.08.007>
- Harmon JK, Slade MA, Vélez RA, Crespo A, Dryer MJ, et al., Radar mapping of Mercury's polar anomalies, *Nature* 369, 213-215 (1994). <https://doi.org/10.1038/369213a0>
- Hartmann WK, Terrestrial, lunar, and interplanetary rock fragmentation, *Icarus* 10, 201-213 (1969). [https://doi.org/10.1016/0019-1035\(69\)90022-0](https://doi.org/10.1016/0019-1035(69)90022-0)
- Haruyama J, Ohtake M, Matsunaga T, Morota T, Honda C, et al., Lack of exposed ice inside lunar south pole Shackleton crater, *Science* 322, 938-939 (2008). <https://doi.org/10.1126/science.1164020>
- Hayne PO, Aharonson O, Schörghofer N, Micro cold traps on the Moon, *Nat. Astron.* 5, 169-175 (2021). <https://doi.org/10.1038/s41550-020-1198-9>
- Hayne PO, Hendrix A, Sefton-Nash E, Siegler MA, Lucey PG, et al., Evidence for exposed water ice in the Moon's south polar regions from Lunar Reconnaissance Orbiter ultraviolet albedo and temperature measurements, *Icarus* 255, 58-69 (2015). <https://doi.org/10.1016/j.icarus.2015.03.032>
- Henriksen MR, Manheim MR, Burns KN, Seymour P, Speyerer EJ, et al., Extracting accurate and precise topography from LROC narrow angle camera stereo observations, *Icarus* 283, 122-137 (2017). <https://doi.org/10.1016/j.icarus.2016.05.012>
- Honniball CI, Lucey PG, Arredondo A, Reach WT, Malaret ER, Regional map of molecular water at high southern latitudes on the Moon using 6 μm data from the Stratospheric Observatory for Infrared Astronomy, *Geophys. Res. Lett.* 49, e2022GL097786 (2022). <https://doi.org/10.1029/2022GL097786>
- Humm DC, Kinczyk MJ, Brylow SM, Wagner RV, Speyerer EJ, et al., Calibration of ShadowCam, *J. Astron. Space Sci.* 40, 173-197 (2023). <https://doi.org/10.5140/JASS.2023.40.4.173>
- Humm DC, Tschimmel M, Brylow SM, Mahanti P, Tran TN, et al., Flight calibration of the LROC Narrow Angle Camera, *Space Sci. Rev.* 200, 431-473 (2016). <https://doi.org/10.1007/s11214-015-0201-8>
- Ingersoll AP, Svitek T, Murray BC, Stability of polar frosts in spherical bowl-shaped craters on the Moon, Mercury, and Mars, *Icarus* 100, 40-47 (1992). [https://doi.org/10.1016/0019-1035\(92\)90016-Z](https://doi.org/10.1016/0019-1035(92)90016-Z)
- Koeber SD, Robinson MS, LROC observations of permanently shadowed regions on the Moon, in the 44th Lunar and Planetary Science Conference, The Woodlands, Texas, 18-22 Mar 2013.
- Koeber SD, Robinson MS, Speyerer EJ, LROC observations of permanently shadowed regions on the Moon, in the 45th Lunar and Planetary Science Conference, The Woodlands, Tx, Mar 17-21 2014.
- Kuiper GP, Interpretation of Ranger VII records, University of Arizona, Communications of the Lunar and Planetary Laboratory, Communications Nos. 58–59 (1965).
- Laferriere KL, Sunshine JM, Feaga LM, Variability of hydration across the southern hemisphere of the Moon as observed by Deep Impact, *J. Geophys. Res. Planets* 127, e2022JE007361 (2022). <https://doi.org/10.1029/2022JE007361>
- Li S, Lucey PG, Milliken RE, Hayne PO, Fisher E, et al., Direct evidence of surface exposed water ice in the lunar polar regions, *Proc. Natl. Acad. Sci.* 115, 8907-8912 (2018). <https://doi.org/10.1073/pnas.1802345115>
- Litvak ML, Mitrofanov IG, Sanin A, Malakhov A, Boynton WV, et al., Global maps of lunar neutron fluxes from the LEND instrument, *J. Geophys. Res. Planets* 117, E00H22 (2012). <https://doi.org/10.1029/2011JE003949>
- Livengood TA, Chin G, Sagdeev RZ, Mitrofanov IG, Boynton WV, et al., Moonshine: diurnally varying hydration through natural distillation on the Moon, detected by the Lunar Exploration Neutron Detector (LEND), *Icarus* 255, 100-115 (2015). <https://doi.org/10.1016/j.icarus.2015.04.004>
- Lucey PG, Neumann GA, Riner MA, Mazarico E, Smith DE, et al., The global albedo of the Moon at 1064 nm from LOLA, *J. Geophys. Res. Planets* 119, 1665-1679 (2014). <https://doi.org/10.1002/2013JE004592>
- Lucey PG, Petro N, Hurley DM, Farrell WM, Prem P, et al., Volatile interactions with the lunar surface, *Geochemistry* 82, 125858 (2022). <https://doi.org/10.1016/j.chemer.2021.125858>
- Malin MC, Bell JE, Cantor BA, Caplinger MA, Calvin WM, et al., Context Camera investigation on board the Mars Reconnaissance Orbiter, *J. Geophys. Res. Planets* 112, E05S04 (2007). <https://doi.org/10.1029/2006JE002808>
- Mandt KE, Greathouse TK, Retherford KD, Randall Gladstone G, Jordan AP, et al., LRO-LAMP detection of geologically young craters within lunar permanently shaded regions, *Icarus* 273, 114-120 (2016). <https://doi.org/10.1016/j.icarus.2015.07.031>
- Martin TD, Atwell MJ, Bussey DBJ, Estes NM, Grott M, et al., S.P. Hopper: in-situ exploration of the Shackleton de Gerlache Ridge, in Lunar Exploration Analysis Group, Laurel, MD, 20-22 Sep 2023.
- Mazarico E, Neumann GA, Smith DE, Zuber MT, Torrence MH, Illumination conditions of the lunar polar regions using LOLA topography, *Icarus* 211, 1066-1081 (2011). <https://doi.org/10.1016/j.icarus.2010.10.030>
- McClanahan TP, Mitrofanov IG, Boynton WV, Chin G, Bodnarik J, et al., Evidence for the sequestration of hydrogen-bearing volatiles towards the Moon's southern pole-facing slopes, *Icarus* 255, 88-99 (2015). <https://doi.org/10.1016/>

- jicarus.2014.10.001
- Miller RS, Lawrence DJ, Hurley DM, Identification of surface hydrogen enhancements within the Moon's Shackleton crater, *Icarus* 233, 229-232 (2014). <https://doi.org/10.1016/j.icarus.2014.02.007>
- Mitchell J, Lawrence S, Robinson M, Speyerer E, Denevi B, Using complementary remote sensing techniques to assess the presence of volatiles at the lunar north pole, *Planet. Space Sci.* 162, 133-147 (2018). <https://doi.org/10.1016/j.pss.2017.07.015>
- Mitrofanov I, Litvak M, Sanin A, Malakhov A, Golovin D, et al., Testing polar spots of water-rich permafrost on the Moon: LEND observations onboard LRO, *J. Geophys. Res. Planets* 117, E00H27 (2012). <https://doi.org/10.1029/2011JE003956>
- Mitrofanov IG, Sanin AB, Boynton WV, Chin G, Garvin JB, et al., Hydrogen mapping of the lunar south pole using the LRO neutron detector experiment LEND, *Science* 330, 483-486 (2010). <https://doi.org/10.1126/science.1185696>
- NASA, Second Stand Alone Missions of Opportunity Notice (SALMON-2), National Aeronautics and Space Administration, NNH12ZDA006O (2016a).
- NASA, Element Appendix (PEA) T: hosted payloads on Korea Pathfinder Lunar Orbiter (KPLO), National Aeronautics and Space Administration, NNH12ZDA006O-KPLO (2016b).
- NASA Advisory Council, Lunar Science Workshop: NASA Advisory Council workshop on science associated with the Lunar Exploration Architecture (NASA, Washington, DC, 2007).
- National Academies of Sciences, *Origins, Worlds, and Life: A Decadal Strategy for Planetary Science and Astrobiology 2023-2032* (National Academies Press, Washington, DC, 2022).
- National Academy of Sciences, *Vision and Voyages for Planetary Science in the Decade 2013-2022*, (National Academies Press, Washington, DC, 2011).
- National Research Council, *The Scientific Context for Exploration of the Moon* (National Academies Press, Washington, DC, 2007).
- Neish CD, Bussey DBJ, Spudis P, Marshall W, Thomson BJ, et al., The nature of lunar volatiles as revealed by Mini-RF observations of the LCROSS impact site, *J. Geophys. Res.* 116, E01005 (2011). <https://doi.org/10.1029/2010JE003647>
- Neumann GA, Cavanaugh JF, Sun X, Mazarico EM, Smith DE, et al., Bright and dark polar deposits on Mercury: evidence for surface volatiles, *Science* 339, 296-300 (2013). <https://doi.org/10.1126/science.1229764>
- Noda H, Araki H, Goossens S, Ishihara Y, Matsumoto K, et al., Illumination conditions at the lunar polar regions by KAGUYA(SELENE) laser altimeter, *Geophys. Res. Lett.* 35, L24203 (2008). <https://doi.org/10.1029/2008GL035692>
- Nozette S, Lichtenberg CL, Spudis P, Bonner R, Ort W, et al., The Clementine bistatic radar experiment, *Science* 274, 1495-1498 (1996). <https://doi.org/10.1126/science.274.5292.1495>
- Nozette S, Spudis PD, Robinson MS, Bussey DBJ, Lichtenberg C, et al., Integration of lunar polar remote-sensing data sets: evidence for ice at the lunar south pole, *J. Geophys. Res.* 106, 23253-23266 (2001). <https://doi.org/10.1029/2000JE001417>
- Paige DA, Siegler MA, Harmon JK, Neumann GA, Mazarico EM, et al., Thermal stability of volatiles in the north polar region of Mercury, *Science* 339, 300-303 (2013). <https://doi.org/10.1126/science.1231106>
- Paige DA, Siegler MA, Zhang JA, Hayne PO, Foote EJ, et al., Diviner Lunar Radiometer observations of cold traps in the Moon's south polar region, *Science* 330, 479-482 (2010). <https://doi.org/10.1126/science.1187726>
- Patterson GW, Stickle AM, Turner FS, Jensen JR, Bussey DBJ, et al., Bistatic radar observations of the Moon using Mini-RF on LRO and the Arecibo Observatory, *Icarus* 283, 2-19 (2017). <https://doi.org/10.1016/j.icarus.2016.05.017>
- Pendleton YJ, Water on the Moon, *Proc. Int. Astron. Union.* 11, 402-406 (2015). <https://doi.org/10.1017/S1743921316005652>
- Pieters CM, Goswami JN, Clark RN, Annadurai M, Boardman J, et al., Character and spatial distribution of OH/H₂O on the surface of the Moon seen by M3 on Chandrayaan-1, *Science* 326, 568-572 (2009). <https://doi.org/10.1126/science.1178658>
- Prem P, Artemieva NA, Goldstein DB, Varghese PL, Trafton LM, Transport of water in a transient impact-generated lunar atmosphere, *Icarus* 255, 148-158 (2015). <https://doi.org/10.1016/j.icarus.2014.10.017>
- Robinson MS, Brylow SM, Tschimmel M, Humm D, Lawrence SJ, et al., Lunar Reconnaissance Orbiter Camera (LROC) instrument overview, *Space Sci. Rev.* 150, 81-124 (2010). <https://doi.org/10.1007/s11214-010-9634-2>
- Sanin AB, Mitrofanov IG, Litvak ML, Malakhov A, Boynton WV, et al., Testing lunar permanently shadowed regions for water ice: LEND results from LRO, *J. Geophys. Res. Planets* 117, E00H26 (2012). <https://doi.org/10.1029/2011JE003971>
- Sargeant HM, Bickel VT, Honniball CI, Martinez SN, Rogaski A, et al., Using boulder tracks as a tool to understand the bearing capacity of permanently shadowed regions of the Moon, *J. Geophys. Res. Planets* 125, e2019JE006157 (2020). <https://doi.org/10.1029/2019JE006157>
- Schorghofer N, Gradual sequestration of water at lunar polar conditions due to temperature cycles, *Astrophys. J. Lett.* 927, L34 (2022). <https://doi.org/10.3847/2041-8213/ac5a48>
- Schorghofer N, Williams JP, Martinez-Camacho J, Paige DA, Siegler MA, Carbon dioxide cold traps on the Moon, *Geophys. Res. Lett.* 48, e2021GL095533 (2021). <https://doi.org/10.1029/2021GL095533>
- Shin S, Heo HP, Choi SW, The lunar terrain imager operations concepts, in 2018 SpaceOps Conference, Marseille, France,

28 May-1 June 2018.

- Shoemaker EM, Alderman JD, Borgeson WT, Carr MH, Lugn RV, et al., Progress in the analysis of the fine structure and geology of the lunar surface from the Ranger VIII and IX photographs, Ranger VIII and IX: part 2, experimenters' analyses and interpretations, California Institute of Technology, Jet Propulsion Lab, Technical Report 32-800 (1966).
- Shoemaker EM, Robinson MS, Eliason EM, The south pole region of the Moon as seen by Clementine, *Science* 266, 1851-1854 (1994). <https://doi.org/10.1126/science.266.5192.1851>
- Slade MA, Butler BJ, Muhleman DO, Mercury radar imaging: evidence for polar ice, *Science* 258, 635-640 (1992). <https://doi.org/10.1126/science.258.5082.635>
- Smith DE, Zuber MT, Jackson GB, Cavanaugh JF, Neumann GA, et al., The Lunar Orbiter Laser Altimeter Investigation on the Lunar Reconnaissance Orbiter Mission, *Space Sci. Rev.* 150, 209-241 (2010a). <https://doi.org/10.1007/s11214-009-9512-y>
- Smith DE, Zuber MT, Neumann GA, Lemoine FG, Mazarico E, et al., Initial observations from the Lunar Orbiter Laser Altimeter (LOLA), *Geophys. Res. Lett.* 37, L18204 (2010b). <https://doi.org/10.1029/2010GL043751>
- Speyerer EJ, Boyd A, Mahanti P, Robinson MS, Denevi B, Illuminating the darkness: photometric analysis under diffuse lighting, in European Lunar Symposium, Padua, Italy, 27-29 Jun 2023.
- Speyerer EJ, Povilaitis RZ, Robinson MS, Thomas PC, Wagner RV, Quantifying crater production and regolith overturn on the Moon with temporal imaging, *Nature* 538, 215-218 (2016a). <https://doi.org/10.1038/nature19829>
- Speyerer EJ, Lawrence SJ, Stopar JD, Gläser P, Robinson MS, et al., Optimized traverse planning for future polar prospectors based on lunar topography, *Icarus* 273, 337-345 (2016b). <https://doi.org/10.1016/j.icarus.2016.03.011>
- Speyerer EJ, Robinson MS, Persistently illuminated regions at the lunar poles: ideal sites for future exploration, *Icarus* 222, 122-136 (2013). <https://doi.org/10.1016/j.icarus.2012.10.010>
- Speyerer EJ, Wagner RV, Robinson MS, Licht A, Thomas PC, et al., Pre-flight and on-orbit geometric calibration of the lunar reconnaissance orbiter camera, *Space Sci. Rev.* 200, 357-392 (2016c). <https://doi.org/10.1007/s11214-014-0073-3>
- Spudis PD, *The Value of the Moon* (Smithsonian Books, Washington, DC, 2016).
- Spudis PD, Bussey DBJ, Baloga SM, Butler BJ, Carl D, et al., Initial results for the north pole of the Moon from Mini-SAR, Chandrayaan-1 mission, *Geophys. Res. Lett.* 37, L06204 (2010). <https://doi.org/10.1029/2009GL042259>
- Spudis PD, Bussey DBJ, Baloga SM, Cahill JTS, Glaze LS, et al., Evidence for water ice on the moon: results for anomalous polar craters from the LRO Mini-RF imaging radar, *J. Geophys. Res. Planet.* 118, 2016-2029 (2013). <https://doi.org/10.1002/jgre.20156>
- Stefanov WL, Vanderbloemen LA, Lawrence SJ, The I4 Online Query Tool for Earth observations data, in International Space Station (ISS) Research and Development Conference, Boston, MA 7-9 Jul 2015.
- Sunshine JM, Farnham TL, Feaga LM, Groussin O, Merlin F, et al., Temporal and spatial variability of lunar hydration as observed by the Deep Impact Spacecraft, *Science* 326, 565-568 (2009). <https://doi.org/10.1126/science.1179788>
- Syal MB, Schultz PH, Riner MA, Darkening of Mercury's surface by cometary carbon, *Nat. Geosci.* 8, 352-356 (2015). <https://doi.org/10.1038/ngeo2397>
- Thomson BJ, Bussey DBJ, Neish CD, Cahill JTS, Heggy E, et al., An upper limit for ice in Shackleton crater as revealed by LRO Mini-RF orbital radar, *Geophys. Res. Lett.* 39, L14201 (2012). <https://doi.org/10.1029/2012GL052119>
- Trang D, Tonkham T, Filiberto J, Li S, Lemelin M, et al., Eruption characteristics of lunar localized pyroclastic deposits as evidenced by remotely sensed water, mineralogy, and regolith, *Icarus* 375, 114837 (2022). <https://doi.org/10.1016/j.icarus.2021.114837>
- Van der Bogert CH, Hiesinger H, Krüger T, McEwen AS, Dundas C, New evidence for target property influence on crater size-frequency distribution measurements, in the 44th Lunar and Planetary Science Conference, The Woodlands, Texas, 18-22 Mar 2013.
- Virkki A, Muinonen K, Radar scattering by planetary surfaces modeled with laboratory-characterized particles, *Icarus* 269, 38-49 (2016). <https://doi.org/10.1016/j.icarus.2016.01.011>
- Watson K, Murray BC, Brown H, The behavior of volatiles on the lunar surface, *J. Geophys. Res.* 66, 3033-3045 (1961). <https://doi.org/10.1029/JZ066i009p03033>
- Wilcoski AX, Hayne PO, Landis ME, Polar ice accumulation from volcanically induced transient atmospheres on the Moon, *Planet. Sci. J.* 3, 99 (2022). <https://doi.org/10.3847/PSJ/ac649c>
- Yoldi Z, Pommerol A, Jost B, Poch O, Gouman J, et al., VIS-NIR reflectance of water ice/regolith analogue mixtures and implications for the detectability of ice mixed within planetary regoliths, *Geophys. Res. Lett.* 42, 6205-6212 (2015). <https://doi.org/10.1002/2015GL064780>
- Zhang JA, Paige DA, Cold-trapped organic compounds at the poles of the Moon and Mercury: implications for origins, *Geophys. Res. Lett.* 36, L16203 (2009). <https://doi.org/10.1029/2009GL038614>
- Zuber MT, Head JW, Smith DE, Neumann GA, Mazarico E, et al., Constraints on the volatile distribution within Shackleton crater at the lunar south pole, *Nature* 486, 378-381 (2012). <https://doi.org/10.1038/nature11216>